
THICKNESS DRIVEN SPIN REORIENTATION IN ULTRATHIN
Fe/Ni(111)/W(110) FILMS

**MAGNETIC SUSCEPTIBILITY OBSERVATION
OF
THICKNESS DRIVEN SPIN REORIENTATION
IN
ULTRATHIN Fe/Ni(111)/W(110) FILMS
BY
GENGMING HE, B.Sc.**

A Thesis

Submitted to the School of Graduate Studies

in Partial Fulfillment of the Requirements

for the Degree

Master of Science

McMaster University

© Copyright by Gengming He, September 2014

MASTER OF SCIENCE (2014)
(Physics and Astronomy)

McMaster University
Hamilton, Ontario

TITLE: Magnetic Susceptibility Observation of Thickness Driven Spin
 Reorientation in Ultrathin Fe/Ni(111)/W(110) Films

AURTHUR: Gengming He, B.Sc (Sichuan University)

SUPERVISOR: Professor David Venus

NUMBER OF PAGES: ix, 98

Abstract

Measurements of SMOKE ac magnetic susceptibility of Fe/Ni(111)/W(110) ultrathin films were used to investigate the thickness driven spin reorientation transition. χ_{\perp} exhibits a broad peak with an exponential decay at high coverage, which is in agreement with the stripe domain model studied in the temperature driven spin reorientation. A strong $\chi_{[001]}$ peak, which comes from the perpendicular-canted state transition, suggests a continuous reorientation process. $\chi_{[001]}$ was measured at T=255K, 300K, 315K, 330K, 360K and 380K. A temperature-thickness phase diagram was constructed and reveals the temperature dependence of the surface anisotropy. The $\chi_{[001]}$ peak magnitude is attenuated by high temperature and vanishes at T=380K. It suggests a "domain melting" in the perpendicular magnetization state. Another χ_{\perp} peak at $t \approx 1.0ML$ correlates to the film formation. A quantitative model is built to explain the microscopic mechanism behind this peak.

Acknowledgements

I would like to express my sincere gratitude to my supervisor Dr. David Venus. He has provided the invaluable guidance with great patience throughout my time in McMaster. Specifically, his positive attitude is a role model for me to follow in my future career and life. My committee members, Dr. Graeme Luke and Dr. Marek Niewczas, have also provided the important suggestions and advice.

I would also thank Marek Kiela for his technical expertise. His supports enables us to do our work. Thanks should also go to Rob D'Ortenzio for teaching me how to operate the setup. I also appreciate the good time I have with friends in the department. Specifically, my lab mates, Peter, Max, Randy, Adrian and Andy, have made the days in the lab much more enjoyable.

In the end, the supports and understanding of my family are always important for me. No words can express my appreciation.

Contents

Abstract	iii
Acknowledgements	iv
List of Figures	v
Chapter 1. Introduction	1
Chapter 2. Theory	4
2.1 Magnetic moment, magnetization and susceptibility	4
2.2 Paramagnetism and the Curie's law	7
2.3 Magnetic interactions	10
2.3.1 Dipole Interaction	10
2.3.2 Exchange Interaction.....	11
2.3.3 Spin-orbit interaction	13
2.4 Ferromagnetism.....	14
2.5 Magnetic anisotropy	18
2.5.1 Magneto-crystalline anisotropy.....	18
2.5.2 Shape anisotropy.....	22
2.6 Perpendicular magnetization and stripe domains	24

2.6.1	Magnetic anisotropy in thin film system and perpendicular magnetization	24
2.6.2	The stripe domain pattern in perpendicular magnetization state	26
2.6.3	Energy in a domain wall	29
2.6.4	Domain density and the susceptibility of stripe domain state.....	31
2.7	The thickness driven spin reorientation transition in magnetic thin films	34
2.7.2	The anisotropy space and the anisotropy flow description of the thickness driven SRT	35
2.7.3	The continuous process and discontinuous process	39
Chapter 3.	Experiment methods	43
3.1	Ultra-high vacuum (UHV) preparation	43
3.2	W(110) substrate.....	45
3.3	Film deposition.....	48
3.4	Auger electron spectroscopy	50
3.5	Film thickness calibration by the AES	54
3.6	The surface magneto optic Kerr effect and the susceptibility measurements ..	57
Chapter 4.	Magnetic susceptibility observation of the thickness driven SRT	63
4.1	Characterization of the film.....	63
4.2	Experiment results	69

4.3	The continuous process of thickness driven SRT	72
4.3.1	Exponential decay: the stripe domain state.....	72
4.3.2	The pinning effect	73
4.3.3	χ_{001} peak: the starting point of canted state and the continuous SRT	77
4.3.4	The in-plane [001] anisotropy.....	79
4.3.5	A sketch of continuous SRT.....	82
4.3.6	Approximate phase diagram of continuous SRT	83
4.4	Magnetism during the film formation	87
4.4.1	Influence of the defects in the Ni buffer	87
4.4.2	The magnetic island model for the first layer Fe film formation.....	89
Chapter 5.	Conclusions.....	94
Bibliography	96

List of Figures

- Figure 2.1 A sketch of the magnetic moment. It can be present as a circular current..4
- Figure 2.2 Brillouin function with different J . x is proportional to H/T and y is proportional to total magnetization \mathbf{M}8
- Figure 2.3 The plot of χ vs T in the paramagnetic state. The susceptibility is proportional to $1/T$9
- Figure 2.4 The Weiss model. Interacting spins can be represented by a paramagnet in a molecular field which is generated by surrounding spins 15
- Figure 2.5 Graphical solution of MMs. At temperature T_3 , the slope of function $M(y)$ is too large to have an intersection with Brillouin function other than zero point. Thus the ferromagnetism disappeared. 16
- Figure 2.6 The magnetization versus temperature in the ferromagnetic state. When the temperature is close to T_C , the magnetic ordering is fluctuated by the thermal energy and the net magnetization decays. 17
- Figure 2.7 A sketch of a spin pair. Two parallel spins have an angle φ with the axis.19
- Figure 2.8 Spin pairs on a cubic lattice20
- Figure 2.9 The [011] surface of the simple cubic lattice. The missing spins at the corner reduced the symmetry of the surface spins and induces the surface anisotropy.21
- Figure 2.10 The origin of shape anisotropy. Magnetic "free poles" on the sample surface will form additional magnetic dipole which will result in a demagnetic field that opposite to the magnetization.23
- Figure 2.11 The stripe domains in perpendicular magnetized system. Perpendicular

magnetized domains with opposite magnetization direction arrange alternatively throughout the whole sample.	26
Figure 2.12 2D Stripe domain state. The stripes are along y direction. The width of each stripe is L . The shadow areas represent domain wall with width l	27
Figure 2.13 A sketch of domain wall that spin gradually change its direction from up to down. As spins deviate from easy axis z, domain wall will induce extra anisotropy energy. Furthermore, as there is an angle between neighboring spins, the exchange energy will also be increased.	30
Figure 2.14 N layers film can be projected into one single layer with the sized of each spin extend from S to NS.	错误! 未定义书签。
Figure 2.15 The magnetization process of a thin film in stripe domain state. The susceptibility comes from the domain wall motion.	33
Figure 2.16 The angle dependent free energy of a magnetic thin film with different K_1 and K_2 . (a) $K_1 > 0$ and $K_2 > -12K_1$ (b) $K_1 < 0$ and $K_2 > -12K_1$ (c) $K_1 < 0$ and $K_2 < -12K_1$ (d) $K_1 > 0$ & $K_2 < -12K_1$	36
Figure 2.17 The phase diagram of magnetic thin film system in the anisotropy space. The red lines are the possible trajectories of the thickness driven SRT. Blue circles represent the transition points.	37
Figure 2.18 The free energies of the transition points. (1) Perpendicular-canted transition. (2) Canted-in plane state transition. (3) Metastable-in plane state transition. (4) Perpendicular-metastable state transition.	40
Figure 3.1 The ultra-high vacuum system.	44
Figure 3.2 The STM picture of the substrate surface. The terrace structure can be clearly seen. It is obtained by C. Schmidhals and D. Venus.	46
Figure 3.3 The sketch of the sample holder.	47

Figure 3.4 The sketch of a evaporator.....	49
Figure 3.5 The Auger effect. The high energy electron induced a hole on the core level.....	51
Figure 3.6 The Auger analyzer.....	52
Figure 3.7 An example of W AES spectrum. Two peaks are observed at 160eV and 175eV. The size of 175eV peak is usually used to calibrate the film thickness.	53
Figure 3.8 The W AES spectra for the clean substrate and 1ML coverage	55
Figure 3.9 The substrate Auger signal as a function of the deposition time, under the layer by layer growth assumption.	56
Figure 3.10 The Magneto Kerr effect. Ellipticity is induced into the linearly polarized light incident light after being reflected from a magnetized surface.	57
Figure 3.11 Three geometry of SMOKE: a) polar b) longitudinal c) transverse.	58
Figure 3.12 A sketch of the SMOKE set up.....	60
Figure 4.1 The structure of fcc(111) film and bcc(110)film from Dr. H. Johnston's thesis. In fcc(111) film, atoms are aligned at 35 degree and -55 degree from the surface angle. For bcc(110), the direction for the alignment is 45 degree. An enhanced Auger signal is expected at these directions[29].....	65
Figure 4.2 ARAES data obtained by H. Johnston. It demonstrates that Fe film growing on W (110) has a bcc(110) structure while the structure of Ni films will changes to fcc(111) at the second layer[29].....	66
Figure 4.3 The ARAES of the Fe film on the Ni buffer took by H. Johnston. The Fe film keeps the fcc(111) structure at least up to 3ML[32].....	67
Figure 4.4 Susceptibility signal of 2.2ML Fe/2.0ML Ni/W[110] film obtained by Dr. C.S. Arnold through SMOKE. A perpendicular peak is observed at 250K which	

is followed by a sharp peak in [001] direction[24].	68
Figure 4.5 The susceptibility spectrum measured at different temperature.	71
Figure 4.6 The fitting of the exponential decay. The blue lines are the experiment data and the red dash line is the fitting line. The exponential decay is well fitted by the stripe domain model.	73
Figure 4.7 The domain wall is pinned by the defect.	74
Figure 4.8 A typical susceptibility data presenting the pinning effect	76
Figure 4.9 The perpendicular [111] susceptibility and the in-plane [001] susceptibility obtained at 300K. The sharp in-plane peak occur before the perpendicular peak decays exponentially.	78
Figure 4.10 A draft of the canted-stripe state	79
Figure 4.11 The Curie transition peak of a 4.5ML Fe film in the in-planed [001] direction.	80
Figure 4.12 Figure 4.13 The SMOKE signals with DC field pulse: (a) the applied pulse field is in the[001] direction. Pulses are mark by the arrows. The magnetization is flipped after each pulse and the clear steps in the SMOKE signal is observed in this direction; (b) the applied pulse field has [110] direction. No clear step is observed.	81
Figure 4.14 The thickness driven SRT process.	82
Figure 4.15 The in-plane [001] peaks obtained at different temperatures.	83
Figure 4.16 The approximate phase diagram.	84
Figure 4.17 The magnitude of the in-plane [001] peak versus the temperature.	86
Figure 4.18 The influence of 3D islands on susceptibility. (a) from a high quality	

film used as the control. (b)-(d) are obtained at $T=315\text{K}$	88
Figure 4.19 The model with perpendicular magnetized islands is used to explain the first peak.....	90
Figure 4.20 The (a) experiment data of the first peak comparing with (b) the model predicted first peak.....	92
Figure 4.21 The fit of the first peak.	93

Chapter 1. Introduction

Magnetic thin films have stimulated great interest in the last three decades because of their great potential for application in industry. One example of this is the discovery of giant magnetoresistance (GMR) which greatly improved magnetic storage devices. New spintronic devices being currently developed will continue to rely on magnetic thin film materials. Thus, basic research on magnetic materials, especially magnetic thin films, still have profound value.

Magnetic ultra-thin films are only a few atomic monolayers thick (usually less than 10ML). The reduced symmetry at a film surface or interface in ultra-thin film can result in novel magnetic properties. Neel[1] has predicted theoretically that the magnetization in ultra-thin films will have a surface anisotropy then can lead to a perpendicular magnetic orientation. Further study[2] indicates that increasing the film thickness can drive the orientation of the magnetization back to the in-plane direction. This process is called a spin reorientation transition (SRT). Studying the SRT is an important way to characterize the properties of magnetic ultra-thin films, such as how the magneto-crystalline anisotropy changes with film thickness or temperature.

The development of surface science techniques, like molecular beam epitaxy (MBE) and ultra-high vacuum(UHV) systems have made experimental research on the SRT possible. The SRT driven by temperature[3] and strain[4] have been studied in various systems. Previous members in our group studied the temperature driven SRT in Fe/2ML Ni(111)/W(110) films via the surface magneto Kerr effect(SMOKE) susceptibility

measurements, which was the first report of susceptibility measurement of the SRT for ultra-thin films. The perpendicular susceptibility spectrum χ_{\perp} of 2ML Fe/2ML Ni(111)/W(110) films presents a strong signal with an exponential decay which agrees with the stripe domain model derived by Kashuba and Pokrovsky[5]. Other groups have studied the temperature versus thickness phase diagram of the SRT using magnetic microscopy.

Many questions still remain. The first one is how the perpendicular spins change their orientation to the in-plane direction. Y. Millev and *et al*[6] show that the SRT process can go through either a continuous process via a canted state, or a discontinuous process via a metastable state. The actual process of the SRT in the Fe/2ML Ni(111)/W(110) system is unclear. Secondly, a special "disordering transition" in the perpendicular magnetization state at high temperature is observed in C.S. Arnold's measurement[7]. Because the susceptibility behaviour at this transition is very different from that of the ordinary Curie transition, it may not be a transition between the ferromagnetic state and conventional paramagnetic state. More experimental information is required to understand the nature of this transition.

To answer these questions, the thickness driven SRT is investigated in this thesis. SMOKE susceptibility measurements were performed at different temperatures from 255K to 380K in both perpendicular and in-plane directions. Experimental evidence of a continuous SRT process is obtained and an approximate phase diagram of the perpendicular-canted phase transition is constructed. This phase diagram indicates how the surface anisotropy changes as a function of temperature. More information about the "disordering transition" is obtained. In addition, a model is also built to explain the magnetic properties, as reflected

in the susceptibilities, during the first layer film formation.

This thesis is organized as follows. Following this introduction, the basic theoretical background about magnetization and the SRT is covered in chapter 2. Experiment methods are discussed in chapter three. The recipe for Fe/2ML Ni(111)/W(110) growth has been developed by H. Johnston, the SMOKE technique has been improved by K. Fritsch. Other techniques include UHV preparation and Auger electron spectroscopy(AES). Chapter 4 presents the experiment results and discussion. Conclusions are summarized in chapter 5.

Chapter 2. Theory

2.1 Magnetic moment, magnetization and susceptibility

The magnetic moment $d\boldsymbol{\mu}$ is the most basic element in magnetism. Classically, it can be defined as a current loop I which has area $d\mathbf{S}$ [8], as shown in Figure 2.1

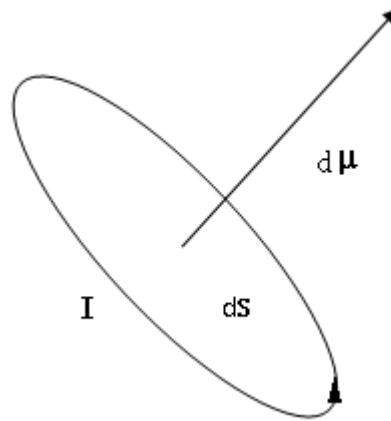


Figure 2.1 A sketch of the magnetic moment. It can be represented as a circular current with an area $d\mathbf{S}$.

$$d\boldsymbol{\mu} = I \cdot d\mathbf{S} \quad (2.1)$$

with unit Am^2 .

An angular momentum, such as orbital momentum \mathbf{L} or spin \mathbf{S} , can be also used to describe the magnetic moment. The connection can be easily seen if we consider the current loop as the result of the circular motion of charged particles.

The size of the atomic magnetic moment can be evaluated by the Bohr model. In this model, the magnetic moment is generated by an electron orbiting a proton. It can be written as

$$\mu_B = -\frac{e\hbar}{2m_e}, \quad (2.2)$$

where the m_e is the mass of electron, \hbar is Planck's constant. Then $\mu_B = 9.274 \times 10^{-24} Am^2$ is the Bohr Magnetron, an useful unit to evaluate atomic magnetic moment.

The magnetic moment is the microscopic basis of magnetism[8]. The magnetic property of a macroscopic system can be regarded as the total effect of all magnetic moments in the system. To evaluate a macroscopic magnetic system, we define the magnetization \mathbf{M}

$$\mathbf{M} = \frac{1}{V} \sum \boldsymbol{\mu} \quad (2.3)$$

It is the volume density of magnetic moments. As a vector, \mathbf{M} not only depends on the size of each magnetic momentum, but also depends on their relative alignment. For example, if all magnetic moments are aligned randomly, the total magnetization \mathbf{M} could be a very small value, or even zero. In contrast, if magnetic momentums are pointing in the same direction, as in a ferromagnetic system, then they can be summed to a large \mathbf{M} .

In statistical mechanics, magnetization is defined as the rate of energy change due to an applied field \mathbf{H} per unit volume[9]. For the system at $T = 0$, we can write

$$M(H) = -\frac{1}{V} \frac{\partial E_0(H)}{\partial H} \quad (2.4)$$

$E_0(H)$ is the ground state energy under the applied field \mathbf{H} . For systems at thermal

equilibrium at temperature T , magnetization is defined as the thermal average of magnetizations of each excited state

$$M(H, T) = -\frac{1}{V} \frac{\sum_n M_n e^{-E_n/k_B T}}{\sum_n e^{-E_n/k_B T}} \quad (2.5)$$

where

$$M_n = -\frac{1}{V} \frac{\partial E_n}{\partial H} \quad (2.6)$$

In statistical mechanics, we also defined the Helmholtz free energy F

$$e^{-F/k_B T} = \sum_n e^{-E_n/k_B T} \quad (2.7)$$

Then equation (2.5) can be written as

$$M(H) = -\frac{1}{V} \frac{\partial F}{\partial H} \quad (2.8)$$

In some special materials, \mathbf{M} is linearly related to the applied field \mathbf{H} when a small field is applied.

$$\mathbf{M} = \chi \mathbf{H} \quad (2.9)$$

These materials are called linear materials. The ratio χ is called the magnetic susceptibility. The magnetic susceptibility describes how easily the system can be magnetized. In general, it is defined as

$$\chi = \frac{\partial M}{\partial H} = -\frac{1}{V} \frac{\partial^2 F}{\partial H^2} \quad (2.10)$$

2.2 Paramagnetism and the Curie's law

The paramagnetic state occurs in system with no, or small, magnetic interactions between spins when temperature is above the Curie temperature T_C . In this state, the magnetic moments have no magnetic ordering and are randomly oriented in the system. Thus, the system as a whole has only a zero total magnetization when no external field is applied. When there is an applied magnetic field, all the magnetic moments will be aligned by the field and present a total magnetization \mathbf{M} parallel to the external field.

First order perturbation theory can be applied to calculate the magnetic properties of the paramagnetic state. According the Ashcroft and Mermin[9], for a system which is formed by atoms or ions with partially filled shell and has non zero J , the energy shift from an applied field can be written as

$$\Delta E_0 = \mu_B \mathbf{H} \cdot \langle JLSJ_z | g(JLS) \mathbf{J} | JLSJ'_z \rangle = \mu_B H g(JLS) J_z \cdot \delta_{J_z J'_z} \quad (2.11)$$

Where $g(JLS)$ is the Landé g -factor and $J_z = -J, -J + 1, \dots, J - 1, J$.

From equation (2.7),

$$e^{-\beta F} = \sum_{J_z=-J}^J e^{-\beta \gamma H J_z} = \frac{e^{\beta \gamma H (J+1/2)} - e^{-\beta \gamma H (J+1/2)}}{e^{\beta \gamma H / 2} - e^{-\beta \gamma H / 2}} \quad (2.12)$$

Where $\beta = 1/k_B T$ and $\gamma = g(JLS)\mu_B$. Then the magnetization can be written as

$$M = -\frac{N}{V} \frac{\partial F}{\partial H} = \frac{N}{V} \gamma J B_J(\beta \gamma J H) \quad (2.13)$$

$B_J(x)$ is Brillouin function defined as

$$B_J(x) = \frac{2J+1}{2J} \coth \frac{2J+1}{2J} x - \frac{1}{2J} \coth \frac{1}{2J} x \quad (2.14)$$

$B_J(x)$ with different J values is plotted in Figure 2.2

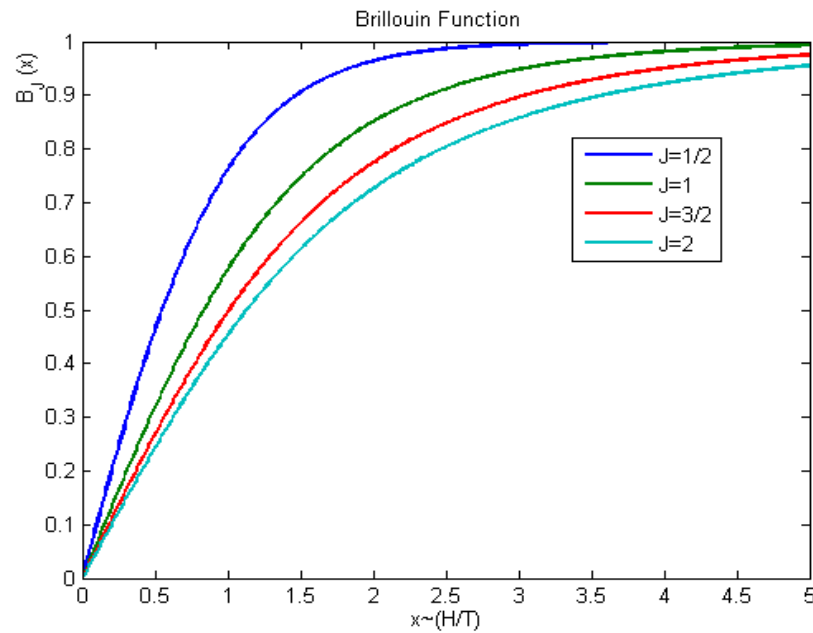


Figure 2.2 Brillouin function with different J . x is proportional to H/T and y is proportional to total magnetization \mathbf{M} .

From Figure 2.2 we can see, when no external field is applied and $x = 0$, the total magnetization equals to zero, as we have discussed. When the external field is strong or the

temperature is small, \mathbf{M} will have the saturation value $\mathbf{M}_s = \frac{N}{V} \gamma J$.

Another important property of the paramagnetic state is described by the Curie's law[9]. At high temperature, x has a small value and the Brillouin function can be expanded as

$$B_J(x) \approx \frac{J+1}{3J} x + O(x^3) \quad (2.15)$$

Then, from equation (2.10), the susceptibility of the system is

$$\chi = \frac{\partial M}{\partial H} = \frac{N}{V} \frac{(g\mu_B)^2}{3} \frac{J(J+1)}{k_B T} \quad (2.16)$$

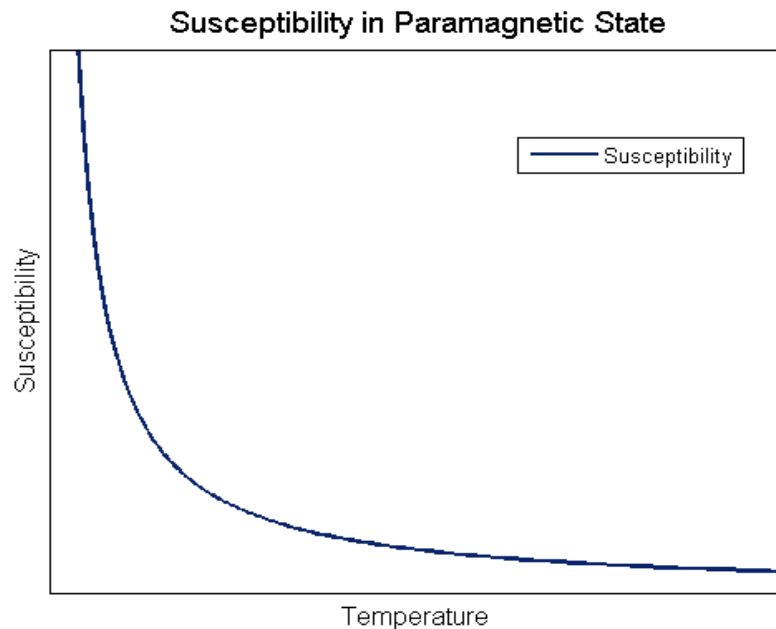


Figure 2.3 The plot of χ vs T in the paramagnetic state. The susceptibility is proportional to $1/T$.

Figure 2.3 sketches this relation. Thus, in the paramagnetic state, the susceptibility of the

system is proportional to $1/T$. In the more general case, the paramagnetic susceptibility has form

$$\chi \sim (T - T_C)^{-\gamma} \quad (2.17)$$

where γ depends on the model and the dimension of the system. T_C is the Curie temperature that the order-disorder phase transition occurs.

2.3 Magnetic interactions

The properties of a magnetic system are dominated by interactions between magnetic moments. In this section, three important magnetic interactions are discussed: Dipole interaction, exchange interaction and spin-orbit interaction.

2.3.1 Dipole Interaction

Two magnetic dipole $\boldsymbol{\mu}_1$ and $\boldsymbol{\mu}_2$ separated by a distance \boldsymbol{r} interact with each other with energy[8]

$$E_d = \frac{\mu_0}{4\pi r^3} [\boldsymbol{\mu}_1 \cdot \boldsymbol{\mu}_2 - \frac{3}{r^2} (\boldsymbol{\mu}_1 \cdot \boldsymbol{r})(\boldsymbol{\mu}_2 \cdot \boldsymbol{r})] \quad (2.18)$$

This energy is approximately in the order of $10^{-23} J$ [8], which is weak compared to other interactions. However the dipole interaction can significantly influence the magnetic properties because of its long interaction range.

2.3.2 Exchange Interaction

The exchange interaction is a strong short range interaction that plays an important role in magnetic ordering. For two spins \mathbf{S}_1 and \mathbf{S}_2 , the Hamiltonian of the exchange interaction between them can be written as[8]

$$\mathcal{H} = -2J\mathbf{S}_1 \cdot \mathbf{S}_2 \quad (2.19)$$

The origin of the exchange interaction is the antisymmetry of quantum mechanical electron wave functions. If we ignore the spin-orbit interaction, then the Hamiltonian of a single electron can be written as $\mathcal{H}_0(\mathbf{r})$ with eigenfunction $\varphi_n(\mathbf{r})\eta_\mu(\boldsymbol{\sigma})$. The orbital function $\varphi_n(\mathbf{r})$ represents the spatial distribution of the electron and the spinor $\eta_\mu(\boldsymbol{\sigma})$ includes information of the spin state [10].

The two-electron Hamiltonian can be written as[10]

$$\mathcal{H} = \mathcal{H}_0(r_1) + \mathcal{H}_0(r_2) + \frac{e^2}{|r_1 - r_2|}, \quad (2.20)$$

where the two electrons interact by the Coulomb potential.

Based on the Hatree-Fock approximation, the two-electron wave function can be constructed by a Slater determinant. Now we define the spatial wave functions φ_a and φ_b with eigenvalue E_a and E_b for the single electron Hamiltonian, respectively; The spinors $\alpha(\boldsymbol{\sigma})$ and $\beta(\boldsymbol{\sigma})$ represent spin-up and spin-down. Then for a system with two spin-up electrons a and b , the wave function of this system can be written as the normalized Slater determinant

$$\varphi_1 = \frac{1}{\sqrt{2}} \begin{vmatrix} \varphi_a(r_1)\alpha(\sigma_1) & \varphi_a(r_2)\alpha(\sigma_2) \\ \varphi_b(r_1)\alpha(\sigma_1) & \varphi_b(r_2)\alpha(\sigma_2) \end{vmatrix} \quad (2.21)$$

It satisfies the antisymmetric property of the Pauli exclusion principle. Similarly, if the electron at state φ_a has spin down, the wave function will be

$$\varphi_2 = \frac{1}{\sqrt{2}} \begin{vmatrix} \varphi_a(r_1)\beta(\sigma_1) & \varphi_a(r_2)\beta(\sigma_2) \\ \varphi_b(r_1)\alpha(\sigma_1) & \varphi_b(r_2)\alpha(\sigma_2) \end{vmatrix} \quad (2.22)$$

The other two eigenfunctions of the two-electron Hamiltonian are

$$\varphi_3 = \frac{1}{\sqrt{2}} \begin{vmatrix} \varphi_a(r_1)\alpha(\sigma_1) & \varphi_a(r_2)\alpha(\sigma_2) \\ \varphi_b(r_1)\beta(\sigma_1) & \varphi_b(r_2)\beta(\sigma_2) \end{vmatrix} \quad (2.23)$$

$$\varphi_4 = \frac{1}{\sqrt{2}} \begin{vmatrix} \varphi_a(r_1)\beta(\sigma_1) & \varphi_a(r_2)\beta(\sigma_2) \\ \varphi_b(r_1)\beta(\sigma_1) & \varphi_b(r_2)\beta(\sigma_2) \end{vmatrix} \quad (2.24)$$

Based on the above four wave functions, the matrix form of two electron Hamiltonian \mathcal{H} is

$$\mathcal{H} = \begin{bmatrix} E_a + E_b + K_{ab} - J_{ab} & 0 & 0 & 0 \\ 0 & E_a + E_b + K_{ab} & -J_{ab} & 0 \\ 0 & -J_{ab} & E_a + E_b + K_{ab} & 0 \\ 0 & 0 & 0 & E_a + E_b + K_{ab} - J_{ab} \end{bmatrix} \quad (2.25)$$

where

$$K_{ab} = \iint dr_1 dr_2 \frac{e^2}{r_{12}} |\varphi_a(r_1)|^2 |\varphi_b(r_2)|^2 \quad (2.26)$$

$$J_{ab} = \iint dr_1 dr_2 \varphi_a^*(r_2) \varphi_b^*(r_1) \frac{e^2}{r_{12}} \varphi_b(r_2) \varphi_a(r_1) \quad (2.27)$$

This matrix has a nondegenerate eigenvalue

$$E_s = E_a + E_b + K_{ab} + J_{ab} \quad (2.28)$$

and a three-fold degenerate eigenvalue

$$E_t = E_a + E_b + K_{ab} - J_{ab} \quad (2.29)$$

Then \mathcal{H} can be represented as

$$\begin{aligned} \mathcal{H} &= \frac{1}{4}(E_s + 3E_t) - (E_s - E_t)\mathbf{S}_1 \cdot \mathbf{S}_2 \\ &= \text{constant} - 2J_{ab}\mathbf{S}_1 \cdot \mathbf{S}_2 \end{aligned} \quad (2.30)$$

Where J_{ab} is the exchange constant between electron 1 and electron 2 which is the energy difference between the singlet and triplet energies.

For a many body system, equation (2.19) can be generalized to

$$\mathcal{H} = -\sum_{\text{n.n.}} J\mathbf{S}_i \cdot \mathbf{S}_j \quad (2.31)$$

The summation is among the nearest neighbours because of the short interaction range of exchange interaction.

2.3.3 Spin-orbit interaction

The spin-orbit interaction is the interaction between the spin and the orbital magnetic momentum.

An electron orbiting the nucleus produces a magnetic field[11], which can be written as

$$\mathbf{B} = -\frac{1}{c^2} \mathbf{v} \times \mathbf{E} = \frac{1}{m_e e c^2 r} \frac{\partial U(r)}{\partial r} \mathbf{L} \quad (2.32)$$

This magnetic field can interact with the magnetic momentum of the spin

$$\boldsymbol{\mu}_s = -g_s \mu_0 \frac{\mathbf{S}}{\hbar} \quad (2.33)$$

Then the interaction energy has the form

$$E_a \sim \mathbf{L} \cdot \mathbf{S} \quad (2.34)$$

2.4 Ferromagnetism

In ferromagnetic state, the exchange interaction causes all the spins to align in the same direction, which results in a spontaneous macroscopic magnetism. In other words, unlike the paramagnetic state, materials in the ferromagnetic state will have a magnetization even where there is no applied field. The Weiss model is widely used to describe ferromagnetism[8].

As we mentioned in the last section, the exchange Hamiltonian for a many body system is

$$\mathcal{H} = -\sum_{ij} J \mathbf{S}_i \cdot \mathbf{S}_j$$

where i and j are limited to the nearest neighbour. We define the molecular field which is generated by spins other than \mathbf{S}_i

$$\mathbf{H}_{mf} = -\frac{2}{g\mu_0\mu_B} \sum_j J\mathbf{S}_j \quad (2.35)$$

Substituting it into exchange Hamiltonian, we have

$$\begin{aligned} \mathcal{H} &= -\sum_j J\mathbf{S}_i \cdot \mathbf{S}_j = g\mu_0\mu_B \mathbf{S}_i \cdot \sum_j J\mathbf{S}_j \\ &= g\mu_0\mu_B \mathbf{S}_i \cdot \mathbf{H}_{mf} \end{aligned} \quad (2.36)$$

Here we induced a uniform molecular field to replace the exchange interaction experienced by spin \mathbf{S}_i . Then the many body interacting system can be regarded as a single paramagnet under the influence of an uniform field, as Figure 2.4. This model is called the Weiss model.

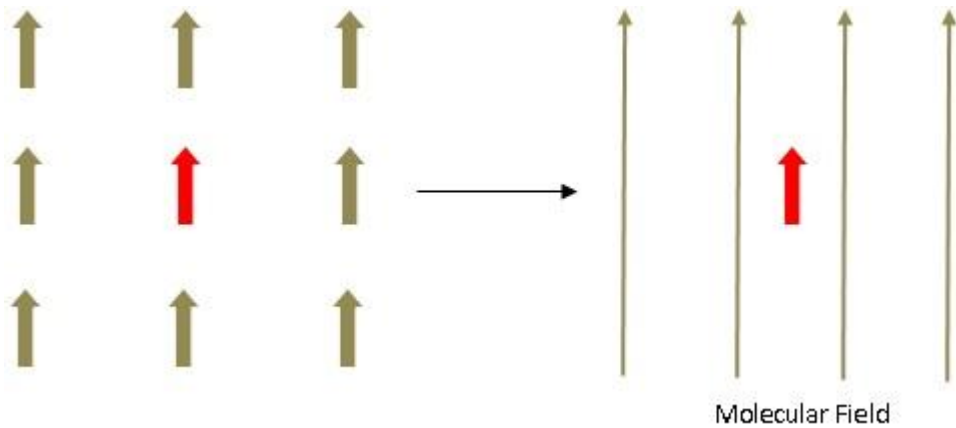


Figure 2.4 The Weiss model. Interacting spins can be represented by a paramagnet in a molecular field which is generated by surrounding spins

In addition, as the molecular field represents the ordering of the system, it must be correlated to the order parameter \mathbf{M} , the magnetization. Thus, we can write

$$\mathbf{H}_{mf} = \lambda \mathbf{M} \quad (2.37)$$

Now we can describe ferromagnetic system as a paramagnetic system. From equation (2.13) we have

$$\frac{M}{M_s} = B_J(y) \quad (2.38)$$

$$y = \frac{g_J \mu_B J H}{k_B T} = \frac{g_J \mu_B J \lambda M}{k_B T} \quad (2.39)$$

Where the applied field H is substituted by the molecular field $\mathbf{H}_{mf} = \lambda \mathbf{M}$.

$\frac{M}{M_s}$ can be solved graphically. The following figure plots the function (2.38), (2.39) at different temperatures.

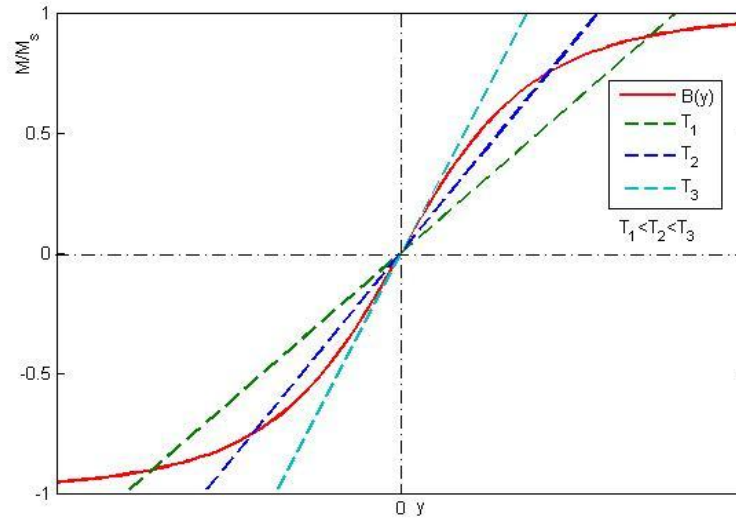


Figure 2.5 Graphical solution of M/M_s . At temperature T_3 , the slope of function $M(y)$ is too large to have an intersection with Brillouin function other than zero point. Thus the ferromagnetism disappeared.

The intersections represent the solution of $\frac{M}{M_s}$. The slope of function (2.39) will increase with temperature. For low temperature, the slope is small and intersects the Brillouin function at a non-zero point, which represents the spontaneous magnetization. However, if the temperature is higher than a critical value T_C , $\frac{M}{M_s}$ will only have one solution at $M = 0$. This indicates that, at high temperature, the system will lose its spontaneous magnetization and transit to paramagnetic state. This transition is called the Curie transition and the critical temperature T_C is called the Curie temperature.

The Curie transition is a result of the competition between the exchange interaction and thermal fluctuations. At high temperature, thermal fluctuations will be strong enough to dominate over the exchange interaction and destroy the magnetic ordering. As a result, the system changes from ferromagnetic state into paramagnetic state where $\chi \propto \frac{1}{T-T_C}$

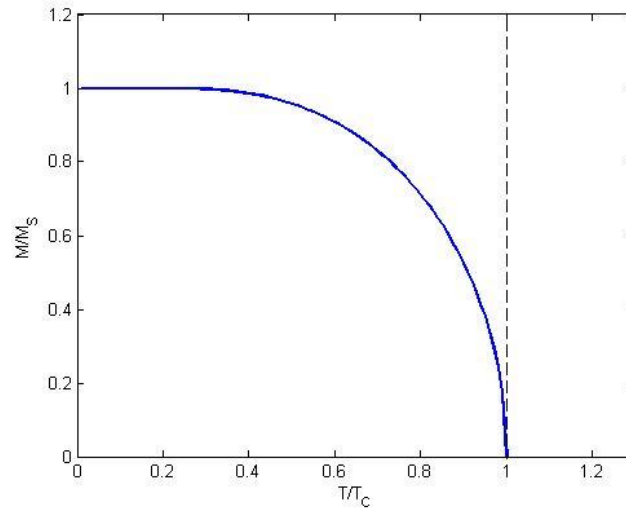


Figure 2.6 The magnetization versus temperature in the ferromagnetic state. When the temperature is close to T_C , the magnetic ordering is fluctuated by the thermal energy and the net magnetization decays.

2.5 Magnetic anisotropy

Magnetic anisotropy refers to the directional preference of the spontaneous magnetization. This preference comes from the magnetization direction dependency of internal energy. This energy term is called anisotropy energy.

Because of the breaking of symmetry of a surface, magnetic anisotropy plays a critical role in ultra-thin film magnetization. In this section, we will discuss two important anisotropies: Magneto-crystalline anisotropy and shape anisotropy. The special case of the magneto-crystalline anisotropy at the thin film surface and how the surface anisotropy is induced by broken symmetry are also discussed.

2.5.1 Magneto-crystalline anisotropy

Magneto-crystalline anisotropy refers to the anisotropy that is related to the crystal symmetry. For example, in hexagonal cobalt system, the spontaneous magnetization prefers the direction of c axis at room temperature.

The magneto-crystalline anisotropy is the result of spin-orbit coupling and has a small size. It arises from the small energy differences when the orientation of the magnetization is changed. It is difficult to calculate from the first principles, but must have the same symmetry as the crystal lattice.

According to Chikazumi[12], a spin-pair model is used to demonstrate the magneto-crystalline anisotropy in metal crystals, as the spins are close and interact directly with each other. A spin pair is sketched in Figure 2.7. φ is the angle between the spin

direction and the bond axis. The interaction energy between the pairing spins depends on the angle φ .

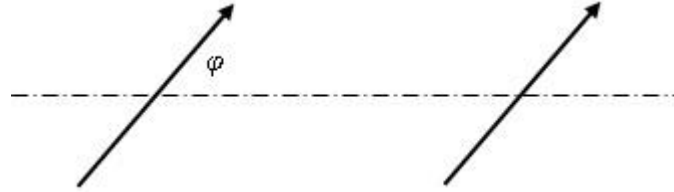


Figure 2.7 A sketch of a spin pair. Two parallel spins have an angle φ with the axis.

The energy of this spin pair can be written as a symmetry-based expansion[12]

$$w(\cos\varphi) = g + l \left(\cos 2\varphi - \frac{1}{3} \right) + q \left(\cos 4\varphi - \frac{6}{7} \cos 2\varphi + \frac{3}{35} \right) \dots \quad (2.40)$$

The constant g corresponds to the normal exchange interaction and is independent on the angle φ . The second term comes from the pseudo-dipolar interaction. The origin of this is the interaction between the partially quenched orbital moment and the spins. The factor l usually has a negative value. The third term comes from the quadrupole interaction.

In the spin-pair model, the magnetic anisotropy is constructed by summing up the energy in all spin-pairs

$$E_a = \sum_i w_i \quad (2.41)$$

Because of the short interaction range, only the interaction between the nearest neighbours are considered. A simple cubic lattice is used as a example to demonstrate how this spin-pair model induces the magneto-crystalline anisotropy. Figure 2.8 is a unit cell of the

simple cubic lattice with spins on each corner. All spins are parallel to each other.

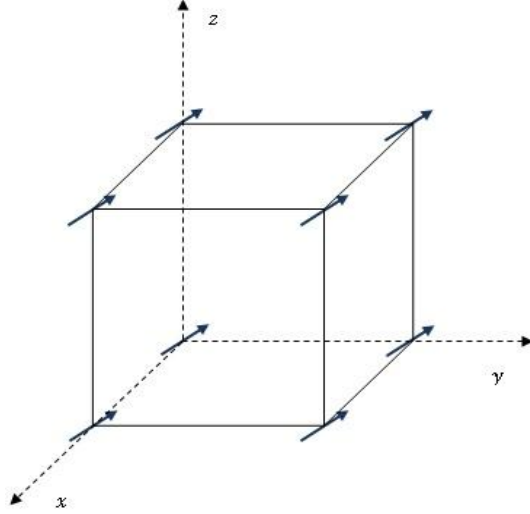


Figure 2.8 Spin pairs on a cubic lattice. We only consider the interaction between the nearest neighbor. $\alpha_1, \alpha_2, \alpha_3$ are defined as the cosine of the angle between spins and the x, y, z axis

We define $\alpha_1, \alpha_2, \alpha_3$ as the cosine of the angle between spins and the x, y, z axis, respectively. Then equation (2.41) can be written as[12]

$$\begin{aligned}
 E_a &= N \left\{ l \left(\alpha_1^2 - \frac{1}{3} \right) + q \left(\alpha_1^4 - \frac{6}{7} \alpha_1^2 + \frac{3}{35} \right) \dots \right. \\
 &\quad \left. + l \left(\alpha_2^2 - \frac{1}{3} \right) + q \left(\alpha_2^4 - \frac{6}{7} \alpha_2^2 + \frac{3}{35} \right) \dots \right. \\
 &\quad \left. + l \left(\alpha_3^2 - \frac{1}{3} \right) + q \left(\alpha_3^4 - \frac{6}{7} \alpha_3^2 + \frac{3}{35} \right) \dots \right\} \\
 &= -2Nq(\alpha_1^2 \alpha_2^2 + \alpha_2^2 \alpha_3^2 + \alpha_3^2 \alpha_1^2) + \text{const.} \quad (2.42)
 \end{aligned}$$

Here the facts $\alpha_1^2 + \alpha_2^2 + \alpha_3^2 = 1$ and $\alpha_1^4 + \alpha_2^4 + \alpha_3^4 = 1 - 2(\alpha_1^2 \alpha_2^2 + \alpha_2^2 \alpha_3^2 + \alpha_3^2 \alpha_1^2)$ are applied. N is the number of spin-pairs in a unit volume.

This shows that, E_a is zero when the magnetization is along $[100]$, $[010]$, $[001]$. When the magnetization is in the $[111]$ direction, $E_a = -2Nq \cdot \frac{3}{4}$, which is smaller. Thus, the anisotropy is induced.

For a thin film system, the broken symmetry on the film surface induces the surface anisotropy. It can be explained by the spin-pair model too. Starting with the simple cubic lattice, the $[011]$ surface is cut, as sketched in Figure 2.9

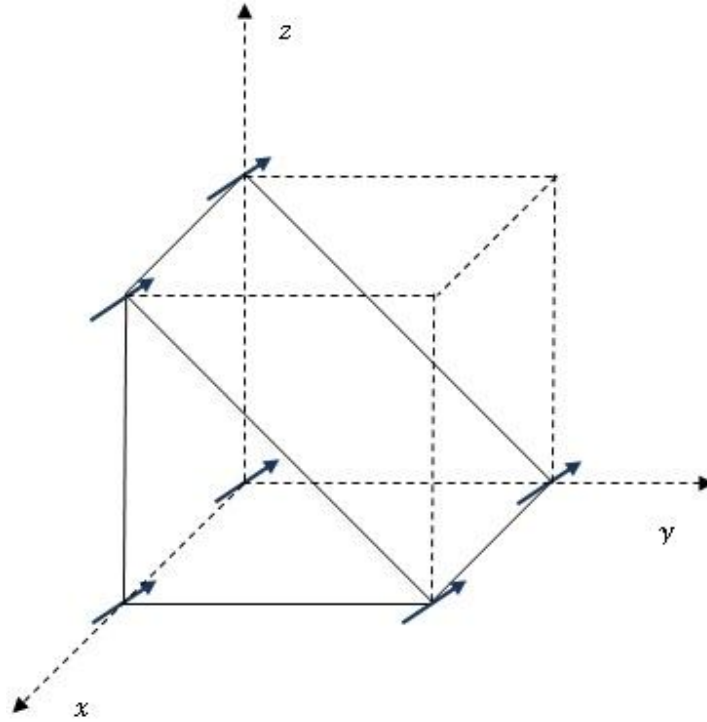


Figure 2.9 The $[011]$ surface of the simple cubic lattice. The missing spins at the corner reduced the symmetry of the surface spins and induces the surface anisotropy.

The missing spins at the upper-right corners reduced the symmetry in y and z direction of the surface spins. Considering the spin-pairs close to the surface, the summation in

equation (2.42) reduces to

$$\begin{aligned}
E_a &= N[l\left(\alpha_1^2 - \frac{1}{3}\right) + q\left(\alpha_1^4 - \frac{6}{7}\alpha_1^2 + \frac{3}{35}\right)\dots \\
&\quad + \frac{1}{2}l\left(\alpha_2^2 - \frac{1}{3}\right) + q\left(\alpha_2^4 - \frac{6}{7}\alpha_2^2 + \frac{3}{35}\right)\dots \\
&\quad + \frac{1}{2}l\left(\alpha_3^2 - \frac{1}{3}\right) + q\left(\alpha_3^4 - \frac{6}{7}\alpha_3^2 + \frac{3}{35}\right)\dots] \\
&= N[(l - \frac{6}{7})(\alpha_1^2 + \frac{1}{2}\alpha_2^2 + \frac{1}{2}\alpha_3^2)] + \text{const.} \quad (2.43)
\end{aligned}$$

As the factor l is negative, E_a is minimized when the magnetization is in the [011] direction, which is perpendicular to the film surface.

Thus, the surface anisotropy is induced in the surface pairs model. The reduced symmetry created a first order spin-orbit interaction term l . This dominates the anisotropy energy, as it is much larger than the second order term in a bulk cubic crystal.

2.5.2 Shape anisotropy

The origin of the shape anisotropy is the long range dipole interaction.

The special case of an uniformly magnetized film is shown in Figure 2.10. The discontinuity of \mathbf{M} on the film surface can be represented by magnetic "monopoles". Those "monopole" pairs can form additional magnetic dipoles[8].

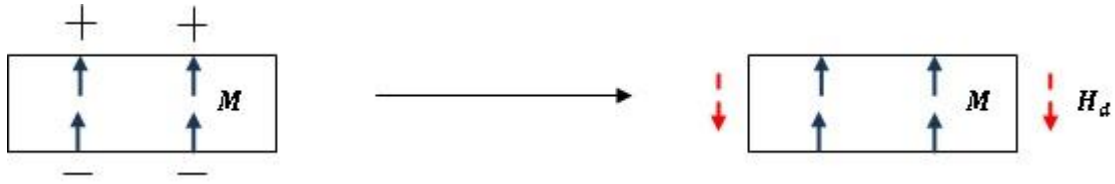


Figure 2.10 The origin of shape anisotropy. Magnetic "free poles" on the sample surface will form additional magnetic dipole which will result in a demagnetic field that opposite to the magnetization.

Those additional dipoles will interact through the dipole interaction. The result of this interaction is equivalent to applying a field antiparallel to the magnetization \mathbf{M} . Thus we call this field as demagnetizing field H_d .

As the density of "monopole" depends on the magnetization \mathbf{M} , H_d should also be proportional to \mathbf{M}

$$\mathbf{H}_d = -N\mathbf{M} \quad (2.44)$$

The minus sign represent the opposite direction between the demagnetization field and the magnetization. N is the demagnetization factor which depends on the direction of magnetization and the shape of the specimen.

For the case of a thin film of infinite lateral extent, the in-plane demagnetizing factor $N_{\parallel} \rightarrow 0$ since the free poles are infinitely far apart. The perpendicular factor $N_{\perp} \rightarrow 1$ in order to meet the microscopic boundary condition of $\mathbf{B} = \mu_0(\mathbf{H} + \mathbf{M})$.

Then the interaction between the demagnetization field and the magnetization is

$$E_d = -\frac{\mu_0}{2V} \int \mathbf{H}_d \cdot \mathbf{M} dv = -\frac{\mu_0}{2V} \int \mathbf{M}_\perp \cdot \mathbf{M} dv \quad (2.45)$$

To minimize this energy, the spontaneous magnetization will have a direction preference, or magnetic anisotropy, which depends on the shape of the specimen.

Specifically, in thin film system, the shape anisotropy is[\[12\]](#)

$$K_{shape} = \frac{1}{2} \mu_0 M^2 \cos^2 \theta \quad (2.46)$$

Where θ is the angle between \mathbf{M} and surface normal. In general, thin film shape anisotropy energy prefers an in-plane magnetization.

2.6 Perpendicular magnetization and stripe domains

2.6.1 Magnetic anisotropy in thin film system and perpendicular magnetization

Perpendicular magnetization is a special phenomenon in thin film systems. It comes from the strong surface anisotropy[\[1\]](#).

In general, the anisotropy energy in a thin film system can be written as

$$E_a = K_1 \sin^2 \theta + K_2 \sin^4 \theta \dots \quad (2.47)$$

Where θ is the angle between the magnetization and the surface normal.

Consider the first leading term in equation (2.47),

$$E_a = K \sin^2 \theta \quad (2.48)$$

In the thin film system, the largest magneto-crystalline anisotropy is the surface anisotropy K_s , since it is first order in the spin-orbit coupling. Thus anisotropy factor K in a thin film can be written as

$$K = \frac{K_s}{t} - \frac{1}{2} \mu_0 M^2 \quad (2.49)$$

Here we ignored the bulk anisotropy which is small in a thin film system. The surface anisotropy is divided by the film thickness t to convert an energy per unit area to an energy per unit volume. The second term is the shape anisotropy constant from the dipole interaction based on the assumption that "magnetic fee poles" are uniformly distributed on film surface. This term induces an in-plane anisotropy.

The strong surface anisotropy induces the perpendicular magnetization. When the film has a small thickness, the first term in equation (2.49) dominates the anisotropy factor and results in a positive K . To minimize the anisotropy energy, the film will have a perpendicular magnetization. In thick films or a bulk system, the influence of the surface anisotropy can be ignored. Then in-plane magnetization will be observed in thick films or bulk samples

Increasing the thickness of a thin film can drive the magnetization to reorient from the perpendicular direction to the in-plane direction. This transition is called the thickness

driven spin-reorientation transition (SRT). It will be discussed in details in the later section.

2.6.2 The stripe domain pattern in a perpendicular magnetization state

A stripe domain pattern usually occurs in thin film systems with a perpendicular magnetization. In this state, perpendicular domains pointing up and down are alternatively arranged in stripes throughout the system, as Figure 2.11 shows. It is a result of reducing the dipole interaction energy.

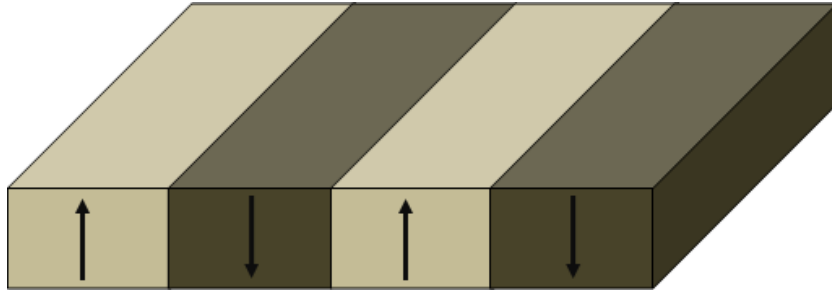


Figure 2.11 A sketch of stripe domains in perpendicular magnetized system. Perpendicular magnetized domains with opposite magnetization direction are arranged alternatively throughout the whole sample. It is the result of balancing the dipole interaction energy and the domain wall energy.

In the perpendicular magnetization state, the dipole interaction energy has the form:

$$\mathcal{H}_{dip} = \frac{\Omega}{4\pi} \sum_{ij} \frac{\mathbf{S}_i \cdot \mathbf{S}_j}{r_{ij}^3} \quad (2.50)$$

which is negative for spin pairs with opposite orientation. Thus, compared to the uniform perpendicular magnetization state, this stripe domain state can significantly reduce the dipole interaction energy[13].

The stripe pattern comes from the competition between the exchange interaction and the dipole interaction. The exchange interaction dominates at short range and near neighbour spins are aligned parallel to each other. For spins with a large distance, the long range dipole interaction dominates and drives them align in opposite direction. Thus, stripe domains are formed.

Kashuba *et.al* [5] calculate the energy gained by forming the stripe pattern in a continuum model.

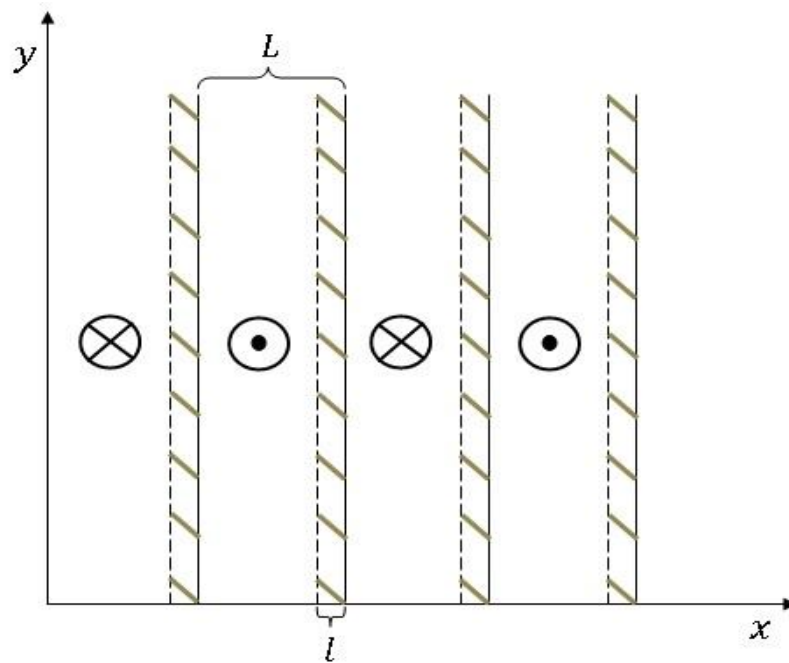


Figure 2.12 A sketch of 2D stripe domain state. The stripes are along y direction. The width of each stripe is L . The shadow areas represent domain wall with width l . The magnetization of neighbouring domains are opposite.

As Figure 2.12 shows, we assume the direction of the spins is independent of y coordinate and y extends to plus-minus infinity. Two type of stripe domains are arranged alternatively

in the x direction. The width of stripes is defined as L . The shadowed area with width l on the boundary between neighbouring domains is the domain wall. The calculation assumes $l = 0$ and ignores the domain wall energy. It will be discussed later.

We assume all the spins have the same size S . Denote \mathbf{S} as spins in domains pointing up(or out) and \mathbf{S}' as spins in domains pointing down (or in). Define \mathbf{S}^0 and \mathbf{S}'^0 as spins in uniform state. Then in a N layers film, the energy difference between the uniform and stripe state can be written as

$$\begin{aligned}\Delta E_d &= \Omega N^2 \sum_{down} \int dx' dy' \sum_{up} \int dx dy \frac{\mathbf{S} \cdot \mathbf{S}' - \mathbf{S}^0 \cdot \mathbf{S}'^0}{|\mathbf{r} - \mathbf{r}'|^3} \\ &= -2\Omega N^2 S^2 \sum_{down} \int dx' dy' \sum_{up} \int dx dy \frac{1}{|\mathbf{r} - \mathbf{r}'|^3} \quad (2.51)\end{aligned}$$

Equation (2.51) contains the change of dipole interaction energy between each up-pointing domain and all other down-pointing domains, and used the fact the that $\mathbf{S} \cdot \mathbf{S}' - \mathbf{S}^0 \cdot \mathbf{S}'^0 = -2S^2$.

Further simplifications are applied on equation (2.51). First of all, for an area with length L_x in x, the number of stripes $N_x = nL_x$, where n is defined as the stripe density. Then the summation of down-pointing stripes can be simplified to

$$\sum_{down} \int dx' = \frac{nL_x}{2} \int_0^{L-l} dx' \quad (2.52)$$

The factor $\frac{1}{2}$ comes from the fact that only half of stripes pointing down. The integrate is limited within 0 to $L - l$ excludes the domain wall areas. The summation of up-pointing domains, as they are separated by down-pointing domains, can be written as

$$\sum_{up} \int dx = \int_L^{2L-l} dx + \int_{2L}^{3L-l} dx + \dots = \sum_{i=odd} \int_{iL}^{(i+1)(L-l)} dx \quad (2.53)$$

For the integrations along y , as spins are independent of the y coordinate, we can assume $y' = 0$, and $\int dy' = L_y$. Where L_y is the length of the sample area in the y direction.

Based on these simplification and assumptions, equation (2.51) can be simplified to

$$\frac{\Delta E_d}{L_x L_y} = -2\Omega N^2 S^2 n \int_0^{L-l} dx' \sum_{i=odd} \int_{iL}^{(i+1)(L-l)} dx \int_{-\infty}^{+\infty} dy \frac{1}{[(x-x')^2 + y^2]^{\frac{3}{2}}} \quad (2.54)$$

and the dipole interaction energy gained in an unit area is

$$\frac{\Delta E_d}{L_x L_y} = -4\Omega N^2 n \ln\left(\frac{2}{\pi n l}\right) = \frac{-4\Omega t^2 n}{b^2} \ln\left(\frac{2}{\pi n l}\right) \quad (2.55)$$

Where t is film thickness and b is the distant between each layer. Then $t = Nb$.

2.6.3 Energy in a domain wall

Domain walls are located at the boundaries of domains, where the magnetization gradually change its direction from one to the other. The domain wall energy includes two parts: 1) The exchange energy between neighbouring spins. 2) The anisotropy energy for spins deviating from the easy axis[12].

$$E_{wall} = E_{exchange} + E_{anisotropy} \quad (2.56)$$

First, we consider a one dimension model of domain wall with width $l = Na$. N is the number of layers in the wall and a is the spacing between each layer.

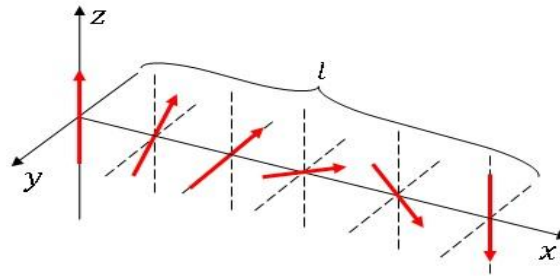


Figure 2.13 A sketch of domain wall that spin gradually change its direction from up to down. As spins deviate from easy axis z , domain wall will induce extra anisotropy energy. Furthermore, as there is an angle between neighboring spins, the exchange energy will also be increased.

Here we define φ as the angle between a spin and the easy axis z . Each spin has the same magnitude S . Then the exchange energy in the domain wall with unit area is

$$E_{exchange} = \frac{JS^2}{a} \int_0^l \left(\frac{\partial \varphi(x)}{\partial x} \right)^2 dx \quad (2.57)$$

From equation (2.48), the anisotropy energy is

$$E_{anisotropy} = \int_0^l K \sin^2 \varphi(x) dx \quad (2.58)$$

Then the wall energy per unit area can be written as

$$E_{wall} = \int_0^l \left\{ K \sin^2 \varphi(x) + A \left(\frac{\partial \varphi}{\partial x} \right)^2 \right\} dx \quad (2.59)$$

Where A is the exchange interaction constant which is defined as $A = \frac{JS^2}{a}$.

The stable domain wall has minimum wall energy. Thus, minimizing the equation (2.59), we have

$$dx = \sqrt{A} \frac{d\varphi}{\sqrt{\sin^2\varphi}} \quad (2.60)$$

Then the domain wall in a 1D model with a unit area of the wall has energy

$$E_{wall} = 2\sqrt{AK} \int_0^\pi \sin\varphi d\varphi = 4\sqrt{AK} \quad (2.61)$$

For domain wall in a two dimensional thin film, the anisotropy factor K in equation (2.61) comes from the surface anisotropy.

$$K = \frac{K_s}{t} \quad (2.62)$$

To get the wall energy per unit area of the film, we must multiple by the film thickness and the energy of domain walls

$$\mathcal{E}_{wall} = ntE_{wall} = 4n\sqrt{AK_s t} \quad (2.63)$$

The factor n is the domain density approximately equals to the number of domain walls in a unit area.

2.6.4 Domain density and the susceptibility of stripe domain state.

As we have discussed, the formation of stripe domain reduces the dipole interaction energy. On the other hand, it also induces domain walls that increase the energy of exchange interaction and anisotropy. Thus, in the stripe domain state, the domain density is determined by balancing these two energy changes.

Combine equation (2.55)(2.63), the domain density can be written as

$$\begin{aligned}
 \Delta E_d &= \mathcal{E}_{wall} \\
 \Rightarrow \frac{-4\Omega t^2 n}{b^2} \log\left(\frac{2}{\pi n l}\right) &= 4n\sqrt{AK_s t} \\
 \Rightarrow n &= \frac{\pi l}{2} \exp\left[-b^2 \sqrt{\frac{AK_s}{\Omega^2} \frac{1}{t^3}}\right] \tag{2.64}
 \end{aligned}$$

From equation (2.64), the domain density n will increase rapidly when the film gets thicker. This relation is observed by C. Won and *etc*[14]. They grow a wedge-like Fe film in which the thickness is changing gradually, on a [100] Cu substrate. Stripe domains are imaged by photoemission electron microscopy. A rapid change of stripe domain density with thickness is observed.

The susceptibility of a thin film in the stripe domain state was studied by Venus and *et al*[15]. It was demonstrated that the susceptibility comes from the domain wall motion. When an external field which is perpendicular to the film surface is applied, stripe domains that have magnetization parallel to the external field will extend by pushing the domain walls. Domains that opposite to the external field will be compressed. Then the film is magnetized as domains parallel to the external field have a larger proportion. This process is displayed in Figure 2.14.

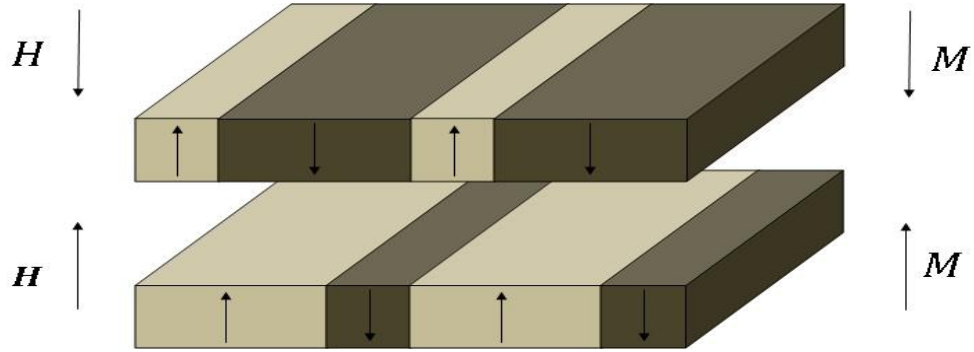


Figure 2.14 The magnetization process of a thin film in stripe domain state. The susceptibility comes from the domain wall motion.

The domain wall motion requires energy. Thus, more energy will be needed to magnetized the film if the domain density is large. As a result, the susceptibility is suppressed. It is demonstrated that the susceptibility is proportional to the inverse of the domain density.

$$\chi \sim \frac{1}{n} \quad (2.65)$$

Combining equation (2.64) and equation (2.65), the relation between the susceptibility and the film thickness can be written as

$$\chi \sim \frac{1}{n} = C \exp \left[b^2 \sqrt{\frac{AK_s}{\Omega^2 t^3}} \right] \quad (2.66)$$

Thus, in the stripe domain state, an exponential decay of susceptibility is expected when the film gets thicker.

2.7 The thickness driven spin reorientation transition in magnetic thin films

A spin Reorientation Transition (SRT) is a phenomenon in which the magnetization changes its direction from one to another. In other words, SRT represent the change of the magnetic easy axis. This phenomenon was first observed in bulk materials at around 1960[16-18] and was widely studied by various methods, like NMR[19], Mossbauer[20] and x-ray photoemission[21] etc.

In a thin film system, the SRT usually means the process where the magnetization changes from perpendicular to the in-plane direction. In some magnetic thin films, the SRT occurs when the film thickness increases. This process is called a thickness driven SRT.

2.7.1 The competition between the surface anisotropy and the dipole interaction

The thickness SRT is a result of the competition between the surface anisotropy energy and the dipole interaction energy. The anisotropy energy in the magnetic thin film can be written as

$$E_a = K_{eff} \sin^2 \theta \quad (2.67)$$

Where $K_{eff} = \frac{K_s}{t} - \frac{1}{2} \mu_0 M^2$ is defined as effective anisotropy which includes the surface anisotropy and the dipole interaction. θ is the angle between the magnetization and the

surface normal. When the thickness t is small, the first surface anisotropy term is large and result in a positive K_{eff} . Then the system should have a perpendicular magnetization to minimized the anisotropy energy. As the thickness increases and beyond a certain value, surface term becomes smaller than the dipole interaction term. Then K_{eff} will be negative and the magnetization should fall into the in-plane direction.

2.7.2 The anisotropy space and the anisotropy flow description of the thickness driven SRT

Yonko and *et al*[22] introduced a more general description of the SRT process based on the anisotropy space and the anisotropy flow theory. The angle dependent free energy of a magnetic thin film can be written as

$$\begin{aligned} F &= F_0 + K_1 \sin^2 \theta + K_2 \sin^4 \theta + \frac{1}{2} \mu_0 M^2 \cos^2 \theta \\ &= \tilde{F} + \tilde{K}_1 \sin^2 \theta + K_2 \sin^4 \theta \end{aligned} \quad (2.68)$$

where $\tilde{K}_1 = K_1 - \frac{1}{2} \mu_0 M^2$. There are three stable states with respect to the magnetization angle that have the minimum free energy: 1) the perpendicular magnetization state where $\theta = 0$; 2) the in-plan magnetization state where $\theta = \frac{\pi}{2}$; 3) the canted magnetization state where $\theta = \arcsin \sqrt{-\tilde{K}_1 / K_2}$. For different \tilde{K}_1 and K_2 values, the relative stability of these three states changes. Figure 2.15 displays the angle dependent free energy at different \tilde{K}_1 and K_2 .

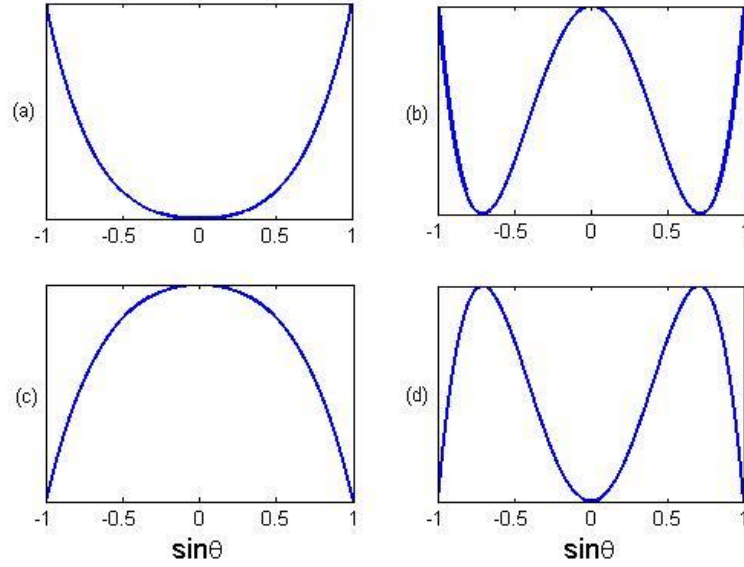


Figure 2.15 The angle dependent free energy of a magnetic thin film with different \widetilde{K}_1 and K_2 . (a) $\widetilde{K}_1 > 0$ and $K_2 > -\frac{1}{2}\widetilde{K}_1$ (b) $\widetilde{K}_1 < 0$ and $K_2 > -\frac{1}{2}\widetilde{K}_1$ (c) $\widetilde{K}_1 < 0$ and $K_2 < -\frac{1}{2}\widetilde{K}_1$ (d) $\widetilde{K}_1 > 0$ & $K_2 < -\frac{1}{2}\widetilde{K}_1$.

Figure 2.15 (a) displays the free energy when $\widetilde{K}_1 > 0$ and $K_2 > -\frac{1}{2}\widetilde{K}_1$. The minimum of the free energy occurs at $\sin\theta = 0$ and the system has a perpendicular magnetization state. The free energy when $\widetilde{K}_1 < 0$ and $K_2 > -\frac{1}{2}\widetilde{K}_1$, as displayed in Figure 2.15 (b), has the minimum when $\sin\theta = \pm\sqrt{-\widetilde{K}_1/K_2}$. Then the system should have a canted state where the magnetization is tilted from the perpendicular direction by an angle $\theta = \arcsin\sqrt{-\widetilde{K}_1/K_2}$. Figure 2.15 (c) is the free energy when $\widetilde{K}_1 < 0$ and $K_2 < -\frac{1}{2}\widetilde{K}_1$. The minimum occurs when $\sin\theta = \pm 1$. Thus the system has an in-plane magnetization state. Figure 2.15 (d) displays the free energy when $\widetilde{K}_1 > 0$ and $K_2 < -\frac{1}{2}\widetilde{K}_1$. In this

region, both perpendicular state and in-plane state have the local free energy minimum. Thus both the perpendicular domain and the in-plane domain coexist in this state. This state is called metastable state.

Based on the above discussion, the phase diagram can be built in anisotropy space using \widetilde{K}_1 and K_2 as coordinates. It is plotted in Figure 2.16.

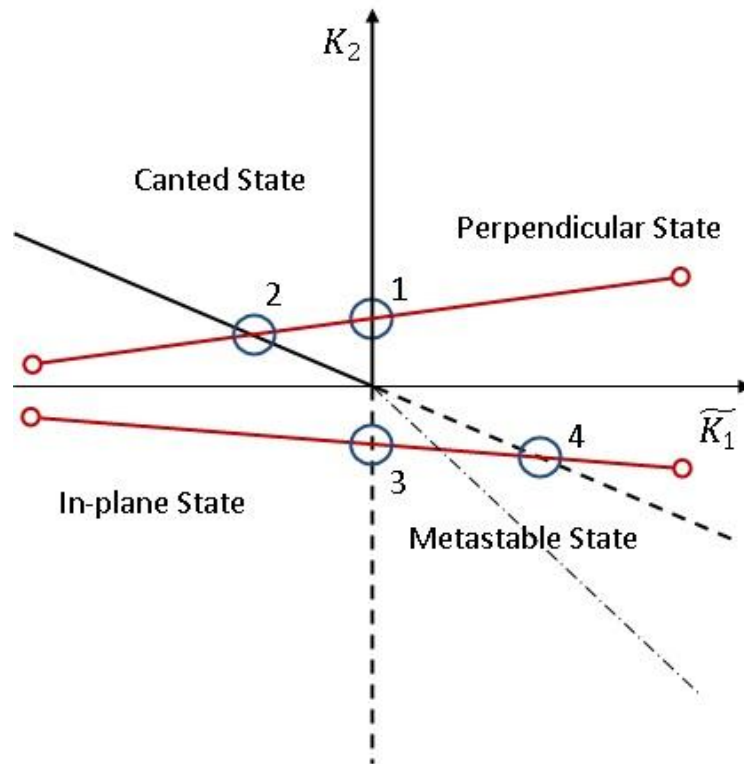


Figure 2.16 The phase diagram of magnetic thin film system in the anisotropy space. The red lines are the possible trajectories of the thickness driven SRT. Blue circles represent the phase transition points.

A dot-dash line $K_2 = -\widetilde{K}_1$ is added in the metastable state. On this line, the perpendicular state and the in-plane state have the same depth in free energy. In the region above this line,

the perpendicular state has deeper free energy, thus is more stable than in-plane state. *Vice versa* in the region below the dot-dash line. It is in agreement with the SRT process. As the system transits from the perpendicular state to the in-plane state through the metastable region, the in-plane domains should dominate at the end of the process.

According to the anisotropy flow theory[6], changing only one variable in the anisotropy factor $K(x_1, x_2, \dots, x_n; t)$, like t for example, and keeping all others constant, the system will move from one state in anisotropy space to another along a monotonic trajectory.

In the anisotropy space, the SRT process can be represent by a monotonic trajectory which connects a point in the perpendicular state region to another in the in-plane state region. Specifically, the trajectory of the thickness driven SRT is a straight line. Based on the fact that the surface anisotropy dominates the anisotropy in thin film systems

$$K_1(T, t) = \frac{K_{1s}(T)}{t} \quad (2.69)$$

$$K_2(T, t) = \frac{K_{2s}(T)}{t} + K_{2v}(T) \quad (2.70)$$

If we keep temperature as a constant, the relation between K_2 and \widetilde{K}_1 in SRT can be written as

$$K_2 = a\widetilde{K}_1 + b \quad (2.71)$$

where

$$a = \frac{K_{2s}}{K_{1s}} \quad (2.72)$$

$$b = \frac{1}{2K_{1s}} \mu_0 K_{2s} M^2 + K_{2v} \quad (2.73)$$

which is a function of a straight line.

2.7.3 The continuous process and discontinuous process

According to Figure 2.16, there are two different thickness driven SRT: the continuous SRT process and the discontinuous SRT process. In the continuous case, the trajectory of the thickness SRT intercepts the positive K_2 axis and the canted state is involved in the process. Through the canted state, perpendicular spins gradually fall into the in-plane direction as the state point approaches the in-plane region along the trajectory. The trajectory of the discontinuous SRT process intercepts at the negative K_2 axis and involves the metastable state. Unlike from the gradual change in the continuous process, in-plane domains will form abruptly when the system goes into the metastable state. As we discussed, the relative stability of in-plane domains and perpendicular domains are different in different areas in the metastable state region. As the system approaches the boundary between the in-plane state and the metastable state, in-plane domains become more stable, thus taking a greater proportion of the system. When the metastable in-plane transition occurs, all the perpendicular domains disappear.

These two process can be easily distinguished by the in-plane susceptibility measurement. Four transition points are marked by the blue rings in Figure 2.16 and their free energies are plotted in Figure 2.17

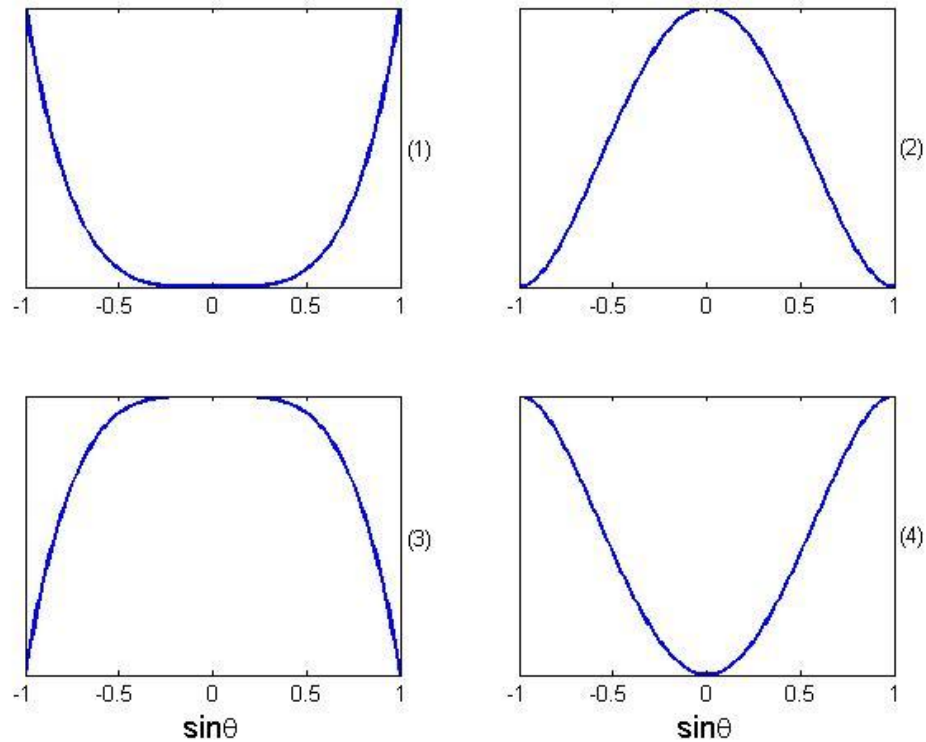


Figure 2.17 The free energies of the transition points. (1) Perpendicular-canted transition. (2) Canted-in plane state transition. (3) Metastable-in plane state transition. (4) Perpendicular-metastable state transition. A wide flat bottom at zero occurs in (1)

The free energy of the perpendicular-canted transition point present a flat minimum at $\sin\theta = 0$. A wide range of θ around zero have free energy minimum. Thus, even when a small magnetic field is applied parallel to the film surface, spins will be easily wiggled and tilted along the field direction. Then an in-plane magnetization parallel to the applied field is induced and a strong in-plane susceptibility signal is expected.

Transition points (2),(4) do not show any flat region in the free energy and a small applied field will not be able to further magnetized the system. Thus, no susceptibility signal is

expected for these two transitions. Transition point (3) for the metastable-in plane transition presents a flat maximum at $\sin\theta = 0$. It also indicates a strong in-plane susceptibility signal which is contributed by the remained perpendicular domains. However, the perpendicular domains almost vanish at the vicinity of metastable-in plane transition point. Thus the susceptibility signal the produced should be tiny and can be ignored.

Venus and *et al* [15] developed a theoretical explanation of the perpendicular-canted transition susceptibility peak. According to MacDonald [23], the magnetic field in the sample is given by

$$\mathbf{H}_{int} = \mathbf{H}_{ext} + \mathbf{H}_{eff} \quad (2.74)$$

where \mathbf{H}_{eff} is the effective field that represents the anisotropy energy. It is defined as

$$\mathbf{H}_{eff} = -\left(\frac{1}{\mu_0}\right) \frac{\partial E_{anis}(\mathbf{M})}{\partial \mathbf{M}} \quad (2.75)$$

Taking the derivative of \mathbf{H}_{int} with respect to \mathbf{M} , we have

$$\left(\frac{\partial \mathbf{M}}{\partial \mathbf{H}_{ext}}\right)^{-1} = \left(\frac{\partial \mathbf{M}}{\partial \mathbf{H}_{int}}\right)^{-1} + \frac{1}{\mu_0} \frac{\partial^2 E_{anis}(\mathbf{M})}{\partial \mathbf{M}^2} \quad (2.76)$$

which can be rearranged as

$$\frac{\partial \mathbf{M}}{\partial \mathbf{H}_{ext}} = \frac{\frac{\partial \mathbf{M}}{\partial \mathbf{H}_{int}}}{1 + \frac{1}{\mu_0} \frac{\partial^2 E_{anis}(\mathbf{M})}{\partial \mathbf{M}^2} \frac{\partial \mathbf{M}}{\partial \mathbf{H}_{int}}} \quad (2.77)$$

The in-plane susceptibility corresponds to $\mathbf{H}^{in-plane}$ and $\mathbf{M}^{in-plane} = \mathbf{M} \sin \theta$. Substituting it into (2.77), we have

$$\chi_{ext}^{in-plane} = \frac{\chi_{int}^{in-plane}}{1 + \frac{1}{\mu_0 M^2} \frac{\partial^2 E_{anis}}{\partial (\sin \theta)^2} \chi_{int}^{in-plane}} \quad (2.78)$$

As we discussed, the anisotropy energy has the form

$$E_{anis} = \widetilde{K}_1 \sin^2 \theta + K_2 \sin^4 \theta \quad (2.79)$$

Thus

$$\frac{1}{M^2} \frac{\partial^2 E_{anis}}{\partial (\sin \theta)^2} = \frac{2}{M^2} \cdot \widetilde{K}_1 + \frac{12}{M^2} \cdot \sin^2 \theta \cdot K_2 \quad (2.80)$$

For the perpendicular state, $\sin \theta = 0$. Equation (2.80) changes to

$$\frac{\partial^2 E_{anis}}{\partial (M \sin \theta)^2} = \frac{2}{M^2} \cdot \widetilde{K}_1 \quad (2.81)$$

Substitute it into equation (2.78), it changes to

$$\chi_{ext}^{in-plane} = \frac{\chi_{int}^{in-plane}}{1 + \frac{1}{\mu_0 M^2} \cdot \frac{2}{M^2} \cdot \widetilde{K}_1 \cdot \chi_{int}^{in-plane}} = \frac{1}{\frac{1}{\chi_{int}^{in-plane}} + \frac{1}{\mu_0 M^2} \cdot \frac{2}{M^2} \cdot \widetilde{K}_1} \approx \frac{1}{\frac{1}{\mu_0 M^2} \cdot \frac{2}{M^2} \cdot \widetilde{K}_1} \quad (2.82)$$

Where the assumption of the large $\chi_{int}^{in-plane}$ is applied. Thus, at the transition point where

$\widetilde{K}_1 = 0$, $\chi_{ext}^{in-plane}$ will diverge.

Chapter 3. Experiment methods

In this chapter, the basic setup and the experiment methods are introduced. Most surface science research is performed in an ultra-high vacuum(UHV) environment to prevent the contaminants. A UHV chamber capable of achieving 10^{-10} torr is used in our experiment which is introduced in section 3.1. Section 3.2 discussed the W substrate. Surface science techniques, including the MBE, AES and SMOKE are introduced in the later sections.

3.1 Ultra-high vacuum (UHV) preparation

Figure 3.1 is a sketch of the UHV system[24]. The vacuum chamber is equipped with three pumps: 1) A rotary pump, which is connected to the chamber through a cold trap right under the vacuum valve. 2) A titanium sublimation pump (TSP) at the bottom of the chamber. It has three Ti-Mo alloy filaments under a titanium plate. As a 45A current goes through one of these filaments, Ti atoms will be sublimated and form a thin film on the plate surface, which will adsorb the gas atoms in the chamber. 3) The ion pump is under the chamber. Gas atoms are ionized by the Penning trap in the ion pump. A strong electrical field which is employed by the ion pump accelerates those ionized gases into a titanium electrode where they are adsorbed.

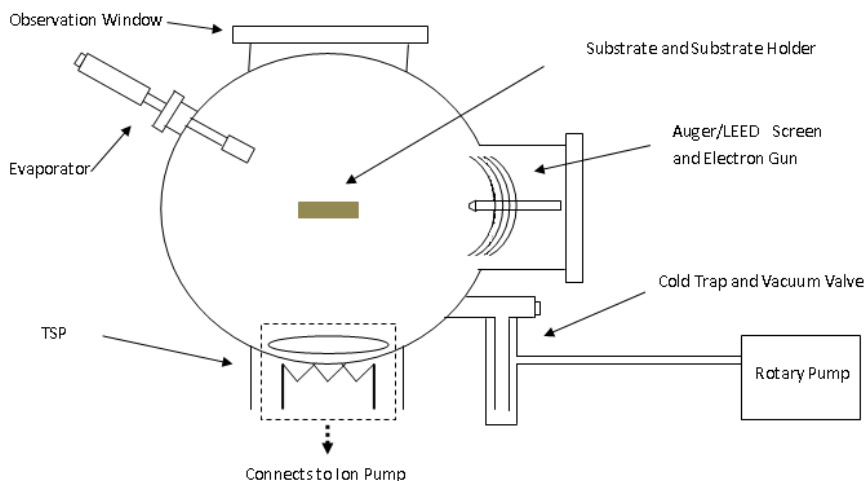


Figure 3.1 The ultra-high vacuum system.

A 2×10^{-10} torr ultra-high vacuum can be achieved by the ion pump. However, the ion pump can only run when the pressure is as low as 10^{-6} torr. Thus the rotary pump engages first. At atmospheric pressure, the vacuum valve is opened and the gases in the chamber are pumped out by the rotary pump. As the pressure decays, rotary pump oil vapor could be "inhaled" into the chamber and contaminate the system. Thus, the cold trap below the chamber vacuum valve is cooled by liquid nitrogen. The oil vapor is liquefied in the cold trap and attaches on its surface. When the pressure achieves 10^{-6} torr, the vacuum valve is closed to isolate the chamber from the lines connecting the rotary pump. The rotary pump keeps running to maintain a low pressure outside the vacuum valve. The ion pump then engages and keeps pumping the gases in the chamber. Moisture and gases attached on the chamber surface is desorbed and pumped away as much as possible by a baking out process that heats the chamber to 150K for 48 hours. After this bake out process, the pressure will drop to 10^{-10} torr. The remaining gas is pumped away by the TSP to achieve

10^{-11} torr. A degassing process is also performed to clean up the gases attached to the sample holder, screens and filaments. The TSP is run daily to maintain the ultra-high vacuum environment in the chamber.

3.2 W(110) substrate

A W single crystal with a (110) surface is selected as the substrate. Using W as the substrate has several advantages. Because W has a large surface free energy, the first layer of a film grown on it wets the surface. Furthermore, the melting point of W is around 3700K. This high melting point permits the substrate surface to be cleaned by flashing the substrate up to 2700K within a few seconds.

The W substrate is directly cut from a W single crystal to $1.1 \times 0.8 \times 0.2 \text{ cm}^3$ [25]. The (110) direction of the substrate surface was determined by Laue x-ray camera with miscut less than 0.4° . Silicon carbide paper, diamond paste and Al_2O_3 vibratory polishing were applied to obtain a highly polished surface. The STM picture of the substrate surface, as Figure 3.2, shows a terrace structure which is not avoidable. The influence of this terrace structure on film magnetic property will be discussed in the next chapter.

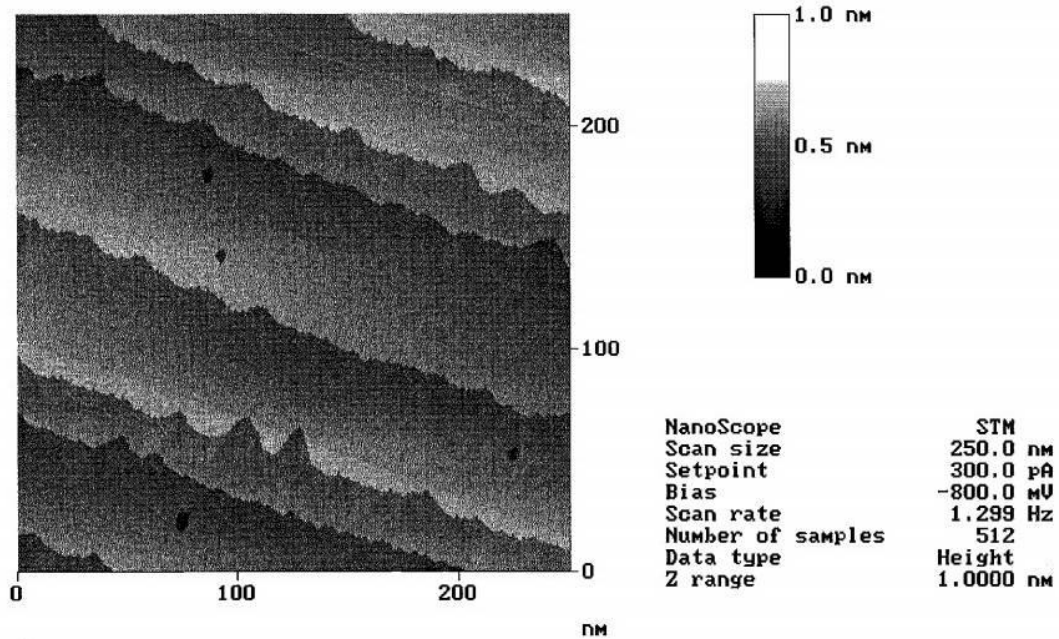


Figure 3.2 The STM picture of the substrate surface. The terrace structure can be clearly seen. It is obtained by C. Schmidhals and D. Venus

The substrate is mounted on a sample holder, as shown in Figure 3.3.

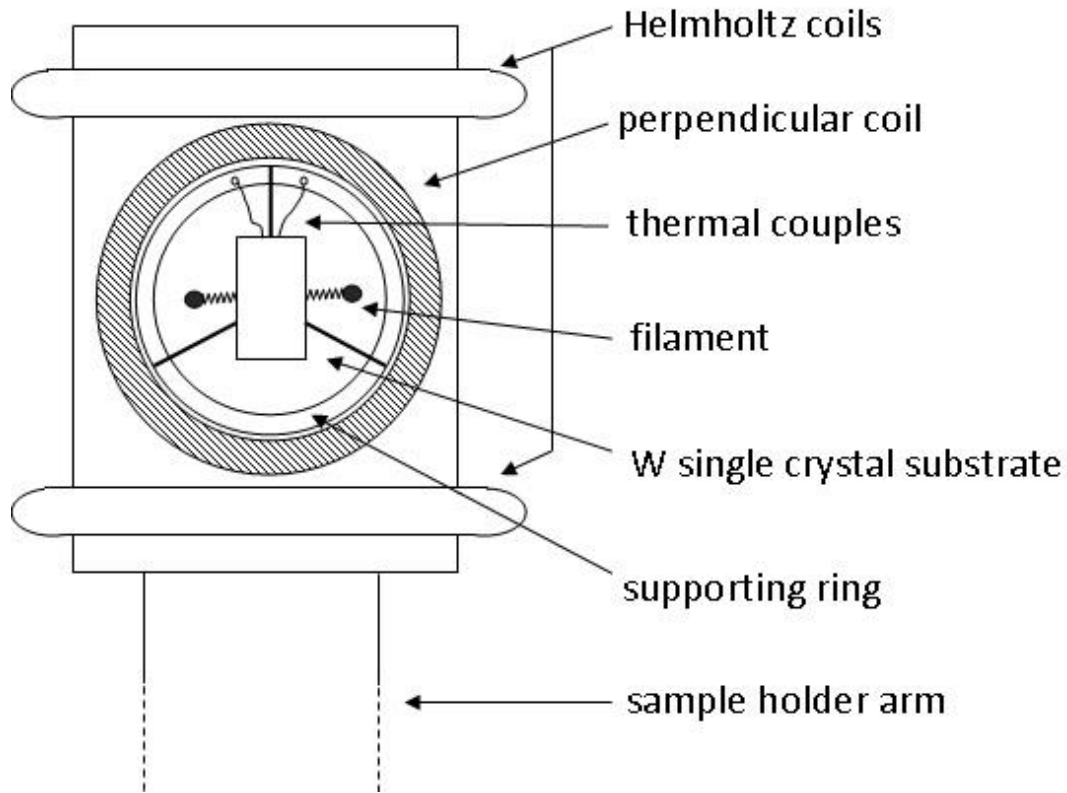


Figure 3.3 The sketch of the sample holder.

The sample holder is connected to a manipulator which can move in the XYZ directions and rotates 360 degree in the XY plane. Thus, the substrate can be freely moved between positions for Auger/LEED, film deposition and susceptibility measurements.

On the sampler holder, the substrate is mounted on a supporting ring which can adjust the azimuthal angle by $\pm 90^\circ$. The supporting ring is placed concentrically in a perpendicular coil. This perpendicular coil and the Helmholtz coils together provide the AC/DC external magnetic field and magnetize the sample in both perpendicular and in-plane directions.

A thermocouple is embedded into the substrate, which can be used to monitor the substrate temperature. The substrate can be heated by a filament under it and be cooled by a copper braid connected to a liquid nitrogen reservoir.

The substrate surface is cleaned by flashing. In the flashing process, a current around 3A goes through the filament under the substrate while a positive 1700V is applied between the substrate and the filament. Thus electrons will be attracted from the filament and bombard the substrate. This bombardment can quickly heat the substrate to around 2600K. The high temperature is maintained for 10s. Most contaminants can be cleaned by flashing. The exception is carbon, as carbon has a large binding energy to W. Thus, carbon is cleaned in a O_2 environment. O_2 is leaked into the chamber under control through a leaking valve. When the pressure increases to 10^{-7} torr, the substrate will be heated to a lower temperature for 30s. C atoms on the surface will be oxidized to CO which has lower binding energy. An ordinary flashing is followed to clean the CO from the surface.

The cleanness of the substrate surface is checked by AES and the LEED pattern.

3.3 Film deposition

Molecular beam epitaxy technique is used to grow the films. With a controlled small deposition rate, multilayer films can be grown on the substrate with a well-defined crystal orientation.

The molecular (atomic) beam is generated through electron beam evaporation. The structure of the evaporator is sketched in Figure 3.4

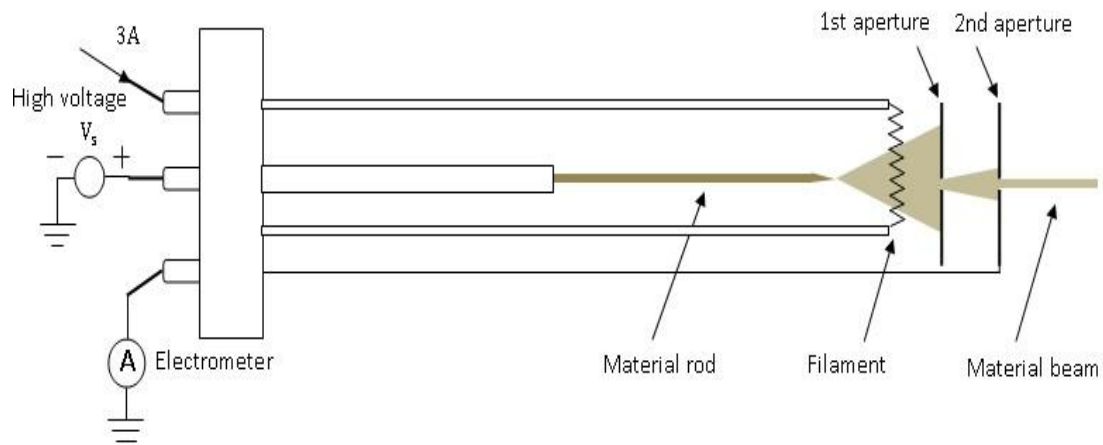


Figure 3.4 The sketch of a evaporator.

An ultra-pure metal rod, like Fe or Ni in this case, is supported rigidly by a metal holder which is connected to a positive high voltage source. A 3A current goes through the filament in front of the metal rod. Then electrons from the filament will be accelerated by the electric field and bombard the tip of the metal rod. The bombardment heats the rod tip to a high temperature that causes the metal to sublime. Two concentric apertures collimate the metal evaporant to provide a metal atom beam with a diameter around 1cm at the sample position. An electrometer is connected to the second aperture. During the bombardment, a certain proportion of evaporant is ionized. This generates a current when the beam hits the second aperture. By monitoring this current(around 1nA), the flux rate of the beam can be obtained. The metal rod can be moved back and forth. The flux rate can be adjusted by controlling the position of the rod tip.

The substrate is usually heated during the film deposition. This deposition temperature is different from film to film. Instead of sticking where they first impinged on the substrate surface, metal atoms diffuse by the thermal energy and find an equilibrium position with a

deep energy well. This scenario is called the equilibrium growth mode.

In equilibrium, three are growth modes observed. In the first case, the film is grown ideally layer by layer. The n th layer growth will not begin until the $n-1$ th layer is complete. This is called Franck-Van der Merwe (FV) growth. Perfect films and interfaces can form under this scenario. Another mode is called 3D growth, or Volmer-Weber (VW) growth. In this mode, films are formed by 3D islands. The third mode is an intermediate case where the first few layers follow a layer-by-layer mode, followed by 3D islands. This is called Stranskii-Krastanov (SK) mode. SK mode is usually observed in actual experiments. By carefully controlling the deposition temperature and deposition rate, SK mode can be close to idealized FV mode.

3.4 Auger electron spectroscopy

Auger electron spectroscopy (AES) is a widely used surface technique. In our measurements, it is used to check the cleanliness of the substrate and measure the film thickness. The AES is based on the Auger effect where Auger electrons with a material-specified energy are emitted when the sample is bombarded by a high energy electron beam. Auger electrons usually have a low energy (10eV-500eV) and have a very short mean-free path, about a few atomic layers. Thus, only Auger electrons from the surface layers can be detected and AES is surface sensitive.

The major process in the Auger effect is the KLL process, as Figure 3.5 shows[25]. The high energy electron beam can eject a core electron. A relaxation will take place where a higher level electron fills the hole in the core level. The energy produced by the relaxation

is carried by the Auger electron which is emitted from the outer shell. Thus, the energy of Auger electron is determined by the sample itself.

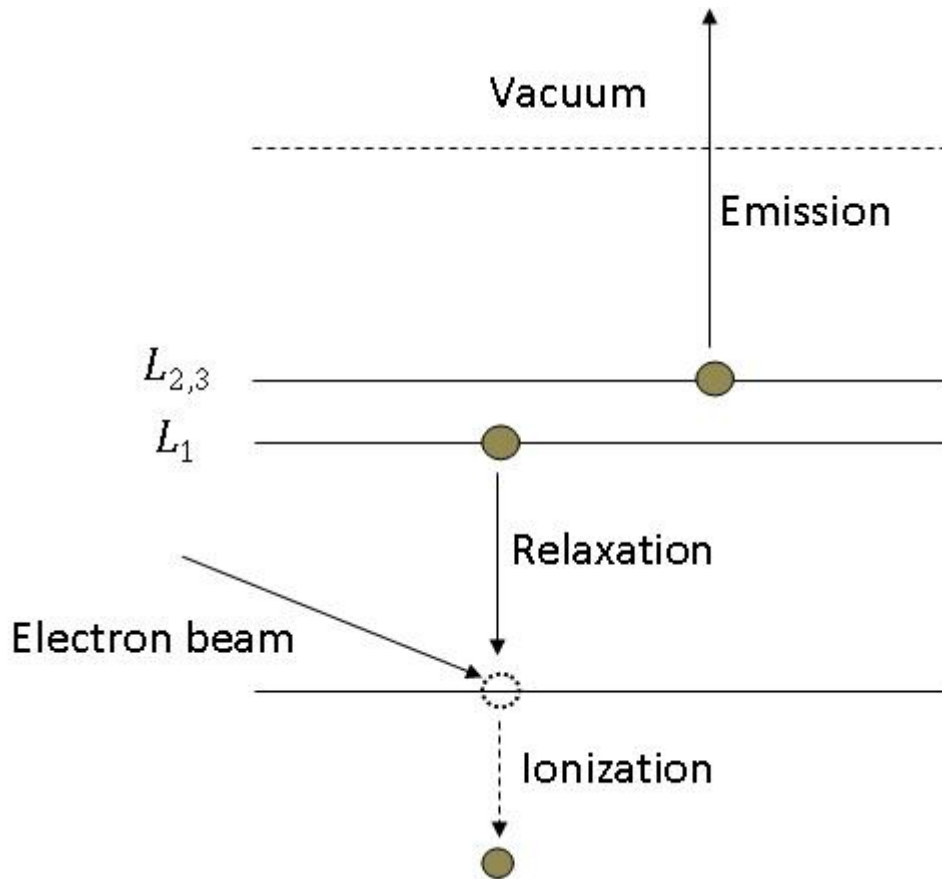


Figure 3.5 The Auger effect. The high energy electron induced a hole on the core level.

The Auger electrons are collected by the Auger/LEED screen which contains a hemispherical analyzer, as Figure 3.6 shows. An ac retarding field E_0 with frequency f is applied between the second and the third analyzer. Thus, only electrons with energy larger than $E_0 \times e$ can be collected. By scanning the retarding field, the spectrum of the number of Auger electron, $N(E > E_0)$, is obtained and Auger electrons will induce a step in the

spectrum.

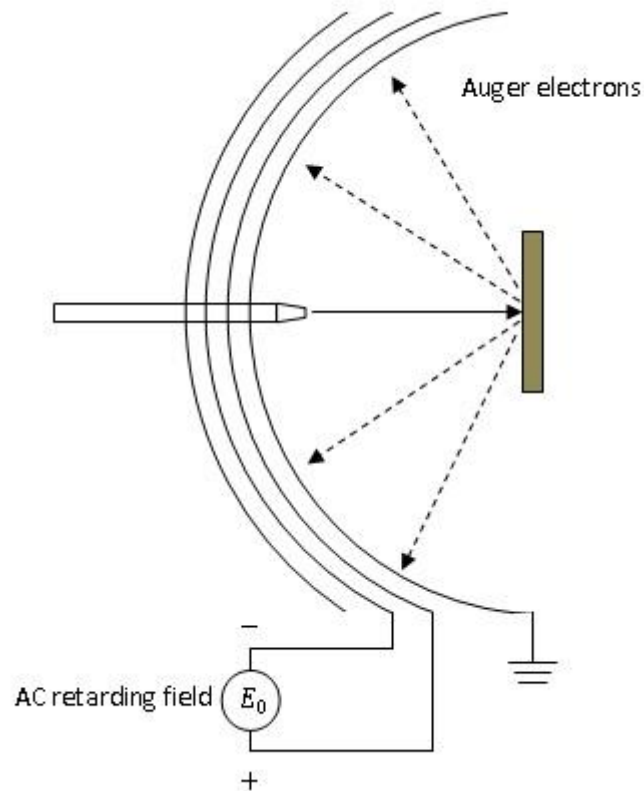


Figure 3.6 The Auger analyzer

However, Auger electrons are not the only electrons emitted from the sample. For example, electrons from the electron gun can also be collected by the analyzer after the multiple inelastic scatterings. Thus, the Auger signal in the $N(E > E_0)$ spectrum is merged with the large and smooth background. To enhance the S/N ratio, the second order derivative of $N(E > E_0)$ with respect to E_0 is obtained by measuring the $2f$ component of the screen current using a lock-in amplifier.

There are two important Auger spectra in our measurements. The first one is the AES of W from 155eV to 190 eV as shown in Figure 3.7. The magnitude α of the 175eV peak of the clean W substrate is an important reference for the film thickness calibration and the cleanliness check. For example, the carbon Auger peak occurs at 273eV and the magnitude of this peak should be controlled within 10% of α .

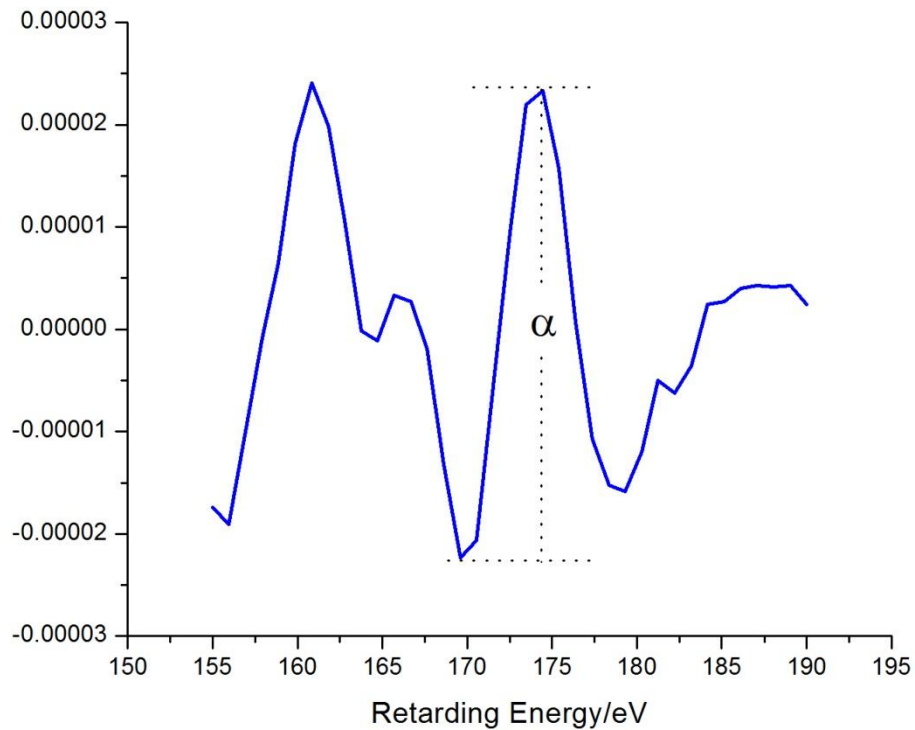


Figure 3.7 An example of W AES spectrum. Two peaks are observed at 160eV and 175eV. The size of 175eV peak is usually used to calibrate the film thickness.

3.5 Film thickness calibration by the AES

W AES is used to calibrate the film thickness. Because of their short mean-free-path, Auger electrons will be attenuated by even a few atomic layers of a film. Thus, a thin film on the substrate reduces the magnitude of the W Auger peak.

We define a transition rate t^n which represent the probability that a substrate Auger electron can penetrate a n-layer thick thin film without any inelastic scattering. Then the intensity of the substrate Auger signal with a n-layers film can be written as [\[26\]](#)

$$I^n = I^0 t^n \quad (3.1)$$

where I^0 is the magnitude of the clean substrate Auger peak. Thus, the measured substrate Auger signal is attenuated, like Figure 3.8 shows.

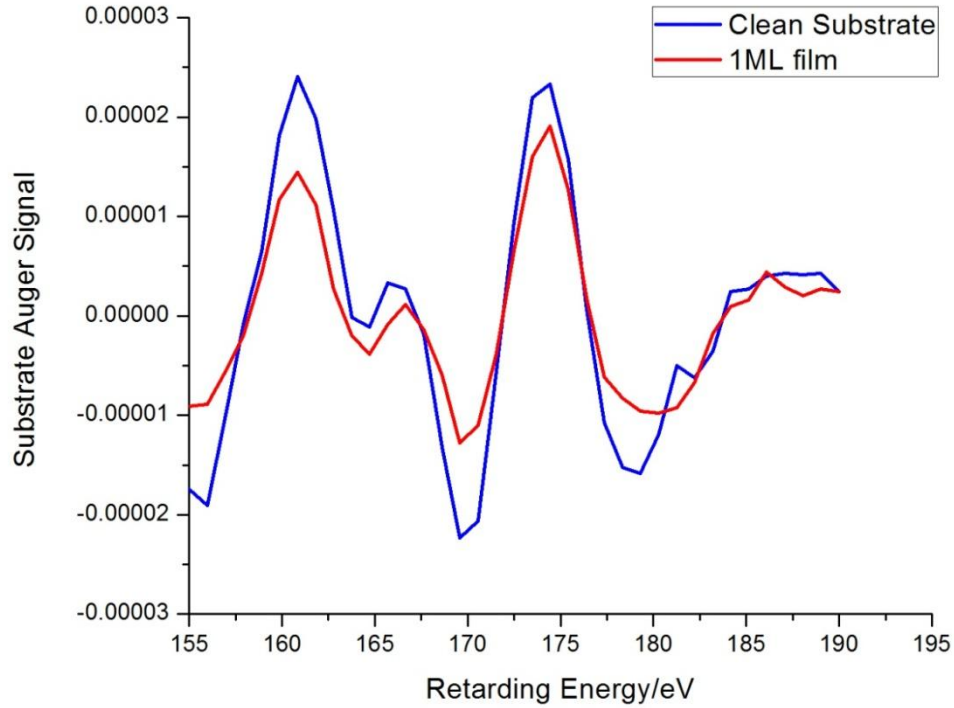


Figure 3.8 The W AES spectra for the clean substrate and 1ML coverage

For layer-by-layer FM growth, define the coverage θ as the fractional completion of the top layer. Then for a film between n layers and $n+1$ layers, the intensity of the substrate Auger signal can be written as[26]

$$I^n = I^0 t^n + I^0 (t^{n+1} - t^n) \theta \quad (3.2)$$

Hence, the Auger signal of the substrate with a film grown layer-by-layer has a linear behaviour between the completion of each layer, as Figure 3.9 shows

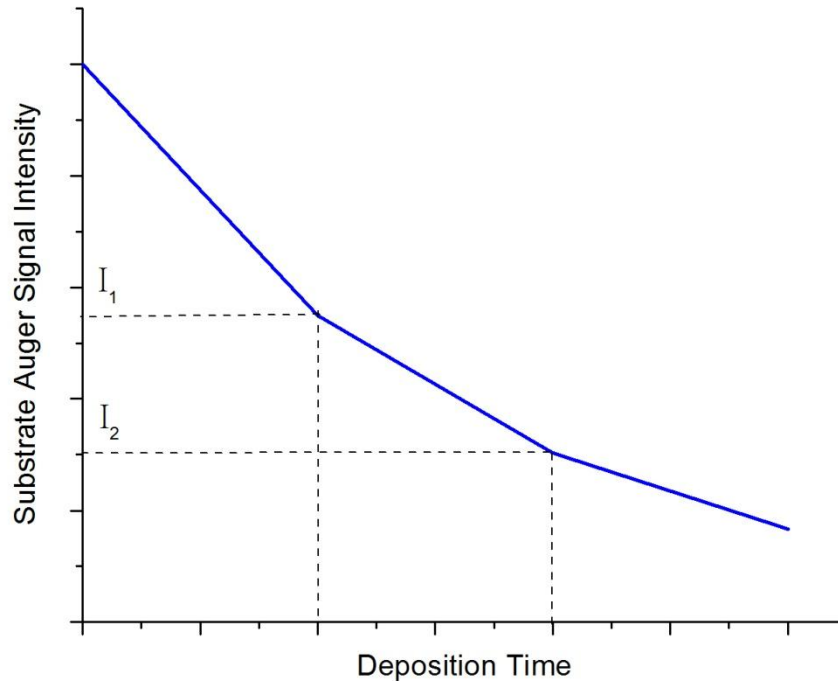


Figure 3.9 The substrate Auger signal as a function of the deposition time, under the layer by layer growth assumption.

Thus, the film thickness can be determined by the substrate AES. In real measurements, this thickness calibration is effective only for the first layer because of the following two reasons: The first reason is the slope differences between higher layers are not as big as the first one. Thus, it is harder to determine the turning point that indicates the formation of the n th layer. Secondly, Figure 3.9 is under the layer-by-layer growth assumption, which is very rare in the real depositions. Small islands in the real deposition can make the turning point ambiguous and further complicate the determination of the completion of higher layer.

In our measurement, AES is used to determine the time t_0 for the deposition of the first layer when the average flux current is I_0 . Define an effective thickness $d_{eff} = I \cdot t$. Then $d_{eff}^1 = I \cdot t_0$ determines the number of atoms in a one layer thick film. The thickness of any thin films is determined by comparing its effective thickness and d_{eff}^1 . A special case is the thickness calibration of a Fe film grown on a Ni buffer. The d_{eff}^1 of Fe film is measured for a bcc (110) Fe film on W substrate. Fe films on a Ni buffer have a fcc(111) structure, which has a 1.3 times larger atom density compared to a bcc(110) film. Thus, the deposition time of each fcc (111) Fe layer should take 1.3 times longer time than an ordinary bcc(110) Fe film.

3.6 The surface magneto optic Kerr effect and the susceptibility measurements

The magnetic properties of thin films are studied by susceptibility measurements based on the surface magneto optic Kerr effect (SMOKE). SMOKE is illustrated in Figure 3.10

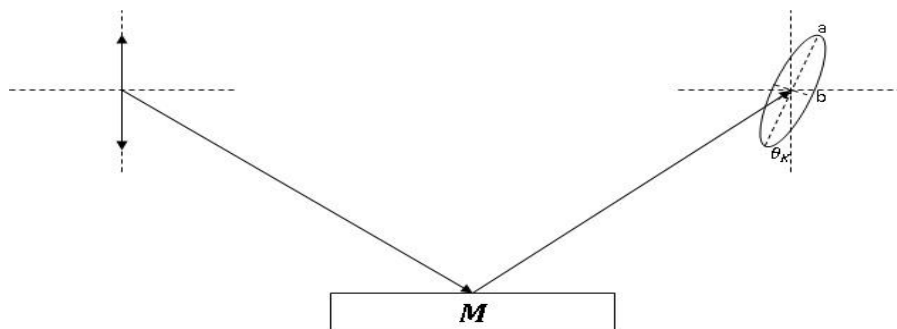


Figure 3.10 The Magneto Kerr effect. Ellipticity is induced into the linearly polarized light incident light after being reflected from a magnetized surface.

After being reflected from a magnetized material, linearly polarized light becomes elliptically polarized with the Kerr rotation θ_K and the Kerr ellipticity ε_K . θ_K is the angle between the major axis of the ellipse and the original polarization plane of the incident light.

The Kerr ellipticity is defined as $\varepsilon_K = \frac{b}{a}$.

There are three basic configurations for the Kerr effect, based on the geometry of the magnetization and the incident light, as Figure 3.11 shows.

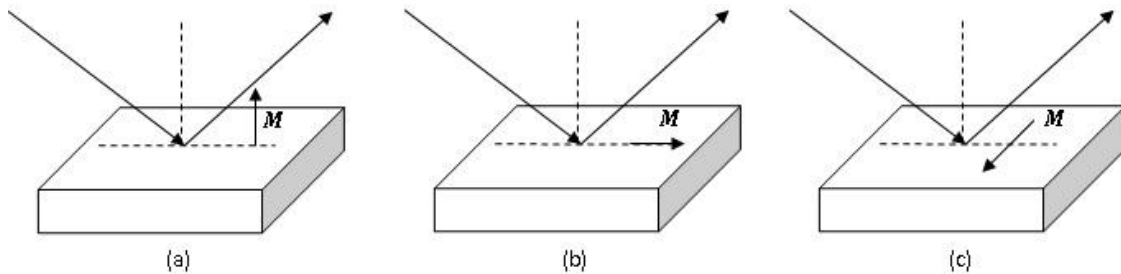


Figure 3.11 Three geometry of SMOKE: a) polar b) longitudinal c) transverse.

Figure 3.11 (a) presents the polar Kerr effect. In the polar geometry, the magnetization is perpendicular to the film surface. Figure 3.11 (b) presents the longitudinal Kerr effect. In the longitudinal geometry, the magnetization is parallel to the film surface and in the incident light plane. Figure 3.11 (c) is the transverse Kerr effect where the magnetization is parallel to the film surface but perpendicular to the incident light plane. In our measurement, only the polar and the longitudinal Kerr effect are used.

The origin of the SMOKE is complicated. Here, the most fundamental principle is discussed as follows:

The magnetization of the sample can induce non-zero terms in the dielectric tensor[24]

$$\epsilon = \begin{pmatrix} 1 & iQ_z & -iQ_y \\ -iQ_z & 1 & iQ_x \\ -iQ_y & -iQ_x & 1 \end{pmatrix} \quad (3.3)$$

where $\mathbf{Q} = (Q_x, Q_y, Q_z)$ is the magneto-optic Voigt parameter which depends on the magnetization. Linearly polarized light can be divided into right circular light and left circular light with the same magnitudes. The magnetization dependent off-diagonal terms in the dielectric tensor can result in a different refractive index for the right circular component $n_R = (1 - \frac{1}{2}\mathbf{Q} \cdot \mathbf{k})$ and the left circular component $n_L = (1 + \frac{1}{2}\mathbf{Q} \cdot \mathbf{k})$. \mathbf{k} is a unit vector along the light propagation direction. Thus, after being reflected from a magnetized surface, the right circular component and the left circular component of the original incident light will have the different phase and magnitude. When they recombine into linearly "polarized" light, this produces the ellipticity and the rotation.

We define the complex Kerr angle $\Phi_K = \theta_K + i\epsilon_K$. The Kerr angle in the polar and longitudinal geometry can be written as[24]

$$\Phi_K^L = \sin(\theta) \left(\frac{4\pi}{\lambda} \right) \left(\frac{n_{sub}}{1-n_{sub}^2} \right) Qd \quad (3.4)$$

$$\Phi_K^R = -\cos(\theta) \left(\frac{4\pi}{\lambda} \right) \left(\frac{n^2}{1-n_{sub}^2} \right) Qd \quad (3.5)$$

Where n_{sub} is the refractive index of the substrate, θ is the incident angle and d is the film thickness. These two relations are only valid for thin films.

The SMOKE set up is sketched in Figure 3.12. The light source is a 2mW HeNe laser. The laser polarization is adjusted by a polarizer mounted on a rotational stage with 1° precision. The laser goes into the chamber through a quartz window W1 and goes out of the chamber through another one W2 after being reflected by the sample. The second polarizer is mounted on another rotational stage which has arcminute precision. The intensity of the laser that passes through the second polarizer is detected by the photodiode.

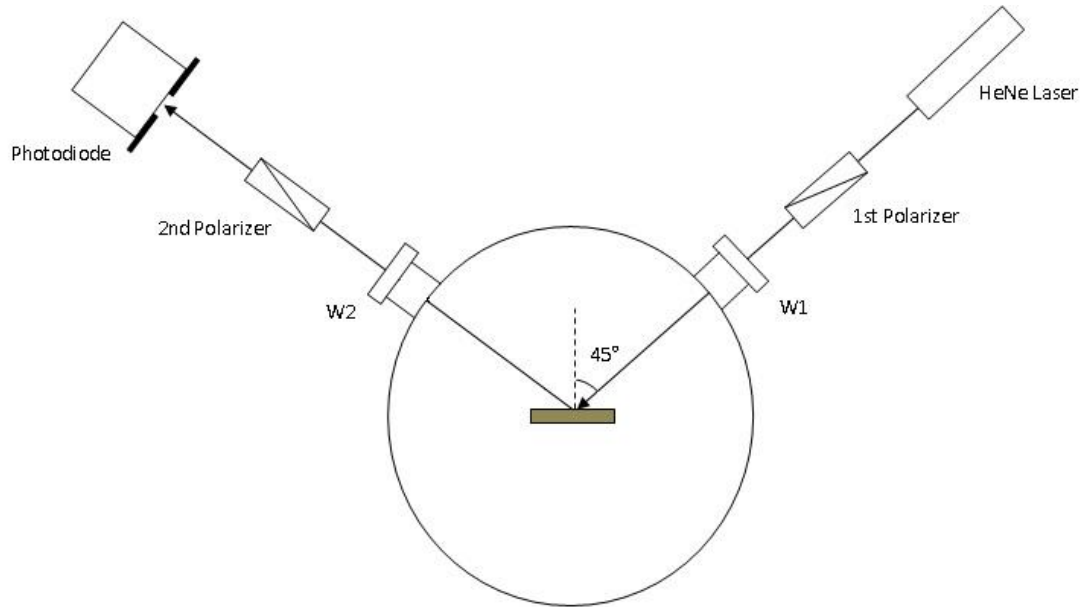


Figure 3.12 A sketch of the SMOKE set up

In general, the intensity of the light passing through two linear polarizer can be written as

$$I(\theta) = I_{max} (\sin^2\theta + \epsilon) \quad (3.6)$$

I_{max} is the light intensity when the two polarizer are parallel, θ is the angle from the extinction where the two polarizer is crossed. ϵ is the extinction ratio which is the ratio

between $I(\theta = 0)$ and I_{max} . For linearly polarized light, ϵ is determined by the quality of the polarizer.

The small change in the polarization from the SMOKE can be detected by the photodiode. It is easy to show that, the SMOKE signal can be written as

$$\frac{\delta I}{I} = \frac{2\delta\theta}{\epsilon^2} \quad (3.7)$$

A ellipticity is produced by the windows W1 and W2 and induces an additional term e in the extinction ratio. Thus, this ellipticity reduces the strength of the SMOKE signal. S. Arnold[27] developed a technique to reduce this ellipticity. The Fresnel reflection coefficient indicates that no ellipticity is induced from the reflection of S or P light with respect to the sample, as they are the eigenpolarizations. Other linearly polarized light will experience a phase shift during the reflection and change into a elliptical light. S. Arnold's technique takes advantage of the ellipticity induced by the reflection to compensate the phase shift from the windows by selecting a specific initial linear polarization which is "slightly displaced from S or P".

The ac susceptibility is measured using this set up. The sample is magnetized by an ac field of 210Hz that is generated by the perpendicular coil or the Helmholtz coils. The signal detected by the photodiode is analyzed by a lock-in amplifier that returns only the portion of signal that has the same frequency as the applied field. Thus, the background noise, which is significant comparing to the SMOKE signal, is reduced.

A study of mechanical noise shows that the signal to noise ratio can be improved by setting

the second polarizer to 24 minutes from extinction[28] for a ac measurement.

The susceptibility is expressed in SI unit system as a unitless quantity. It is written as[28]

$$\chi = \left(\frac{4\pi}{1000}\right) \frac{M^{sat}}{H_a \phi_K^{sat} d} \phi_{ac} \quad (3.8)$$

ϕ_{ac} is the magneto-optic rotation corresponding to the photodiode ac voltage

$$\phi_{ac} = \frac{\Delta I}{2\theta I_{max}} \quad (3.9)$$

Chapter 4. Magnetic susceptibility observation of the thickness driven SRT

The thickness driven SRT in the Fe/2ML Ni fcc(111)/W(110) film was studied by SMOKE ac susceptibility measurements. A 2ML Ni buffer is grown on the W bcc(110) substrate and provides a fcc(111) surface. The Fe thin film grown on top of this buffer follows the fcc(111) structure and presents a perpendicular magnetization at small thickness.

The growth recipe for Fe/2ML Ni fcc(111)/W(110) and its properties were studied by Johnston and Arnold[[25](#), [29](#)]. A short introduction of this system is included in section 4.1. Experimental results of the thickness driven SRT, and their analysis, are discussed in the following sections.

4.1 Characterization of the film

Fcc (111) Fe thin films are a good candidate to observe the SRT, and a Cu(111) substrate has been widely used for fcc (111) Fe thin film preparation. However, the Cu substrate has two major disadvantages. First of all, Fe atoms at the interface can easily diffuse into the Cu substrate. Secondly, instead of growing layer by layer, Fe atoms form 3D islands on the Cu substrate during the film formation. As a result of both of these factors, the structure of a Fe/Cu(111) film is complicated[[30](#)].

To overcome these disadvantages, Johnston developed the following recipe to grow Fe/2ML Ni fcc(111)/W(110) thin films[[31](#)]:

Before deposition, the W substrate surface is cleaned using oxygen to remove carbon contamination. Then, a two-layer Ni buffer is grown. Different growing conditions are used for each layer. The first Ni layer growth is performed with a 550K substrate temperature, followed by a 2 minute annealing procedure at 600K. For the first layer growth, the higher growing temperature and the annealing procedure provides the Ni atoms enough energy to spread out uniformly on the substrate surface and form a smooth and uniform monolayer Ni film. The second Ni layer is grown at 390K without annealing after the growth. Unlike the first layer, Ni atoms at the second layer prefer to form 3D islands. Thus a lower temperature is used to reduce the atom mobility.

The crystalline structure of an ultrathin film is usually determined by the structure of the substrate. This is true for the first layer of Ni. However, for the second layer, the structure of the Ni buffer changes from the bcc(110) to fcc(111).

This structural change has been demonstrated by Johnston via angle resolved Auger electron spectroscopy (ARAES) [29]. In this technique the intensity of Auger electrons is detected at different emission angles with respect to the film surface normal. A strong Auger signal will be detected when the detector is aligned along the direction that atoms are aligned. According to the structure of fcc (111) film and bcc (110) film, as Figure 4.1 shows, the Auger signal should be enhanced at 35 degrees and 55 degrees when the sample has a fcc (111) structure and at 45 degrees for a bcc (110) film

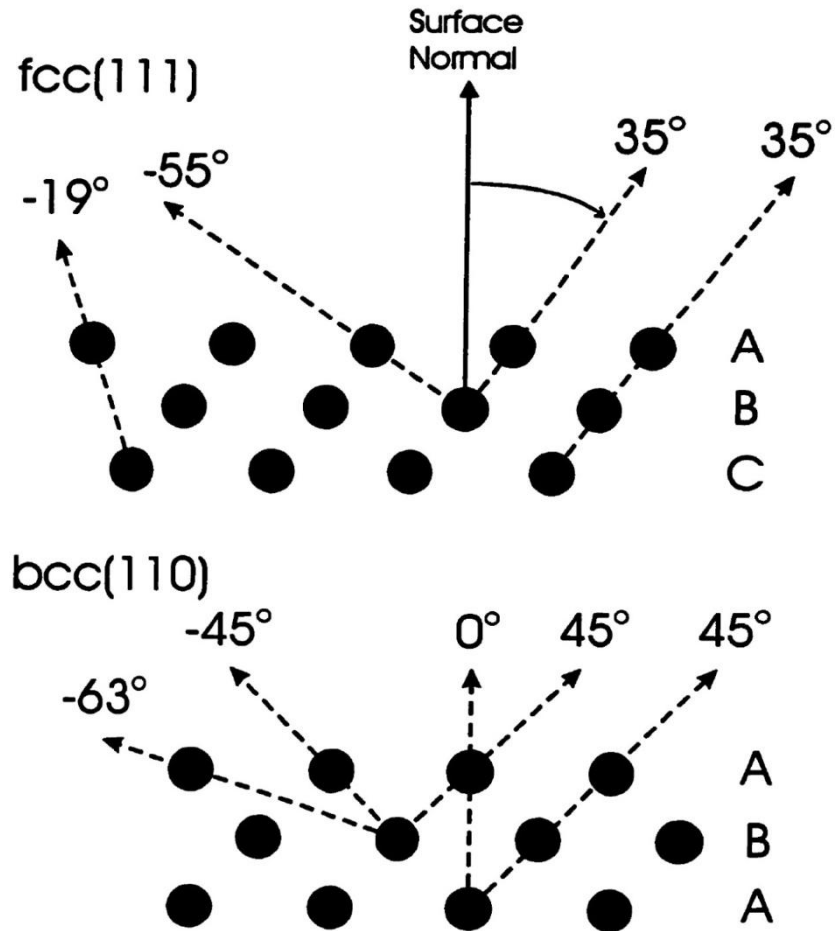


Figure 4.1 The structure of fcc(111) film and bcc(110)film from Dr. H. Johnston's thesis. In fcc(111) film, atoms are aligned at 35 degree and -55 degree from the surface angle. For bcc(110), the direction for the alignment is 45 degree. An enhanced Auger signal is expected at these directions[31].

Figure 4.2 presents the ARAES data taken by Johnston. The upper data comes from a 2.5ML Fe film grow directly on the W(110) substrate, while the lower data comes from the 2.0ML Ni buffer. The 45 degree peak in the Fe film signal indicates its bcc (110) structure. In contrast, peaks at 35 degrees and 55 degrees are clearly observed in the Ni buffer data showing that the second layer Ni buffer has a fcc(111) structure.

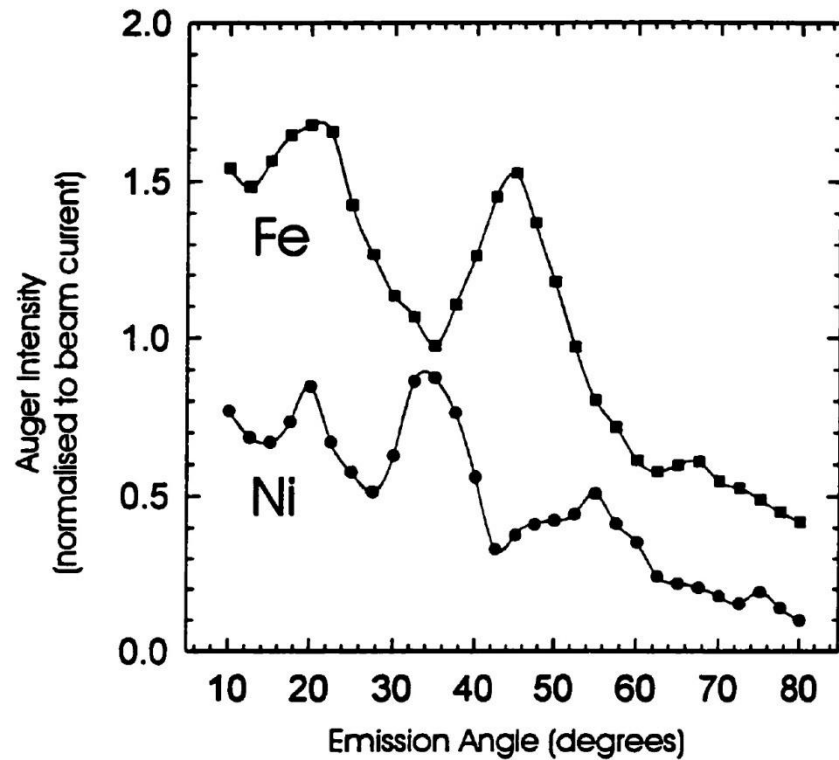


Figure 4.2 ARAES data obtained by H. Johnston. The peaks at 35 degree and 55 degree were observed. It demonstrates that Fe film growing on W (110) has a bcc(110) structure while the structure of Ni films will change to fcc(111) at the second layer[31].

This structural transformation results from the strong strain in the Ni buffer. Normally, Ni crystals have a fcc structure. However, the first layer of the Ni buffer follows the bcc structure of W substrate, which induces a strain that drives the second layer back to the fcc structure.

The Fe films grown on the 2ML Ni buffer keep the fcc (111) structure. This is demonstrated by another ARAES of the Fe film on the Ni buffer, as Figure 4.3 shows. As an Fe crystal is body centred cubic, strain will also drive the Fe film to change its structure gradually from

fcc to bcc. This transition begins at around 4 ML and is completed at 12 ML[29]. Furthermore, Dunlavy[32] also studied the intermixing at the interface between the Fe film and Ni buffer, and showed that this begins when the temperature rises to 400K. To maintain a constant film structure and the magnetic properties, our measurements will be performed below 390K.

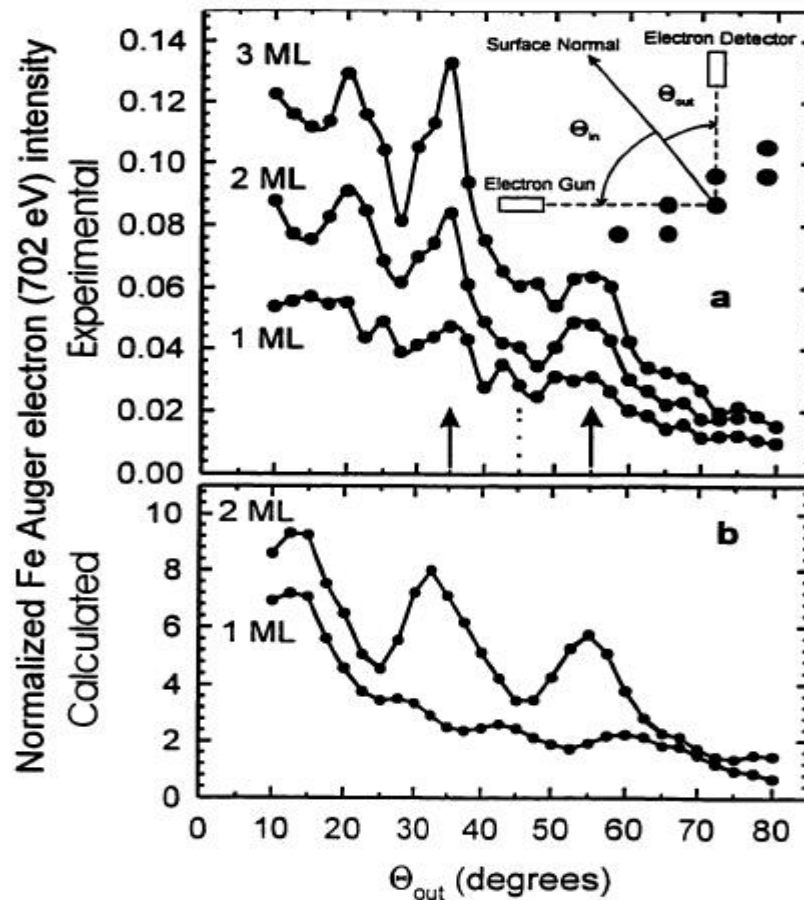


Figure 4.3 The ARAES of the Fe film on the Ni buffer took by H. Johnston. The 35 degree and the 55 degree peaks indicated the Fe film keeps the fcc(111) structure at least up to 3ML[33].

The magnetic properties, especially the spin-reorientation transition as a function of temperature, of this system has been studied by Arnold[7]. Figure 4.4 is the susceptibility of a 2.2ML Fe/2.0ML Ni/W(110) film versus temperature. In Arnold's work, and also in this thesis, the susceptibility components are referent to W crystalline axis.

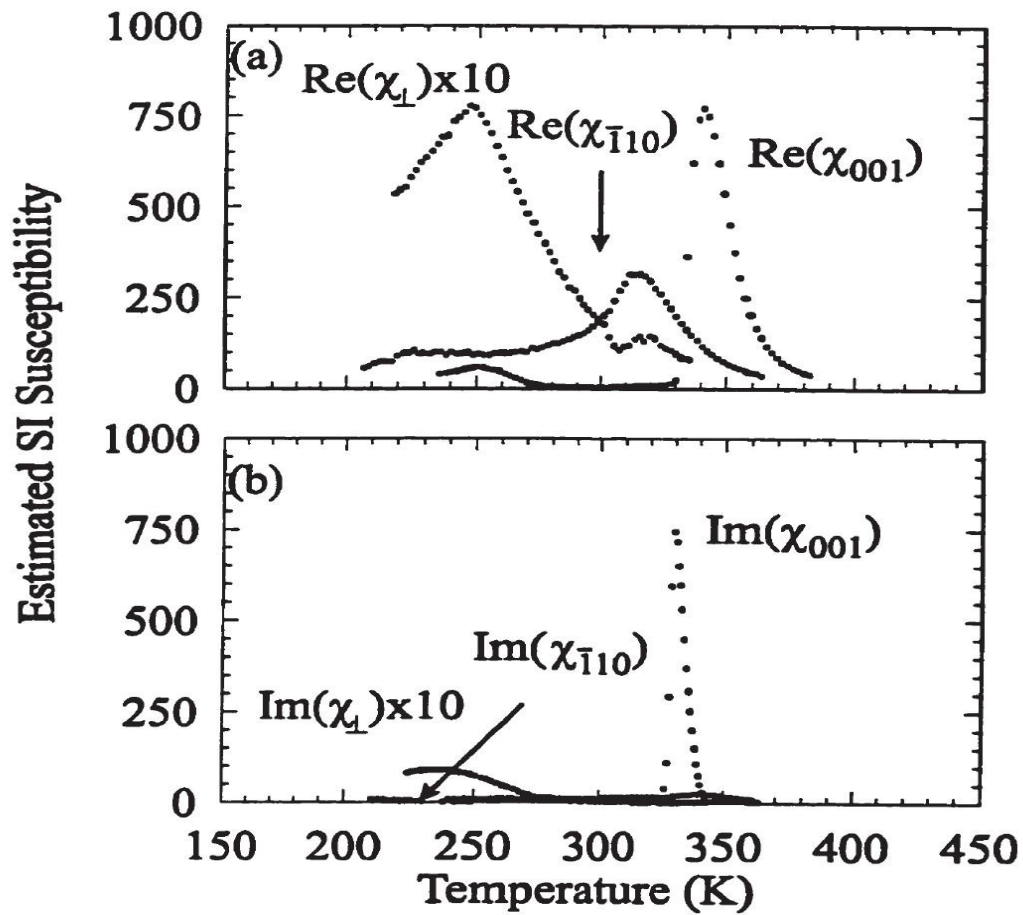


Figure 4.4 Susceptibility signal of 2.2ML Fe/2.0ML Ni/W[110] film obtained by Arnold through SMOKE. A perpendicular peak was observed at 250K which was followed by a sharp peak in [001] direction[25]. The sharp peak represented the in-plane Curie transition. The exponential decay came from the domain wall motion.

Arnold found that the perpendicular peak and the peak in the [001] direction together

represent a SRT process. According to previous theories, stripe domains will form in the vicinity of a SRT point, and the domain density will increase exponentially with temperature. The susceptibility should be proportional to the inverse of domain density and creates an exponential decay. This is in agreement with the experimental perpendicular susceptibility. While the temperature increases, the magnetization falls in-plane. At 350K, a Curie transition occurs and the system transit from in-plane ordered phase into a disordered paramagnetic phase. This phase transition is indicated by the sharp and strong signal in the [001] susceptibility. The Curie transition was not observed in the in-plane $[\bar{1}10]$ susceptibility. This indicates that there is an in-plane magnetic anisotropy and the magnetization has an [001] direction after the SRT.

4.2 Experimental results

The subject of this thesis is the thickness driven SRT in Fe/2ML Ni(111)/W(110) films studied using SMOKE susceptibility measurements. Before Fe film deposition, the 2ML Ni buffer was carefully prepared. Its quality and thickness is controlled and monitored by AES. The laser and the Fe evaporator are carefully aligned to a position where SMOKE and deposition can be performed at the same time. As the available path for the laser is constrained by the laser window and the second polarizer in front of the photodiode, the major adjustments are applied to aligning the Fe evaporator. An additional mechanism is built on the Fe evaporator which allows the adjustment of the direction of evaporation.

The deposition rate of the Fe film is controlled below 0.15ML/min, which is smaller than typical thin film depositions. The small deposition rate allows the film to approach the equilibrium state during the measurement. When a Fe atom hits the Ni buffer, it will take an

relaxation time to relax to a stable position. The measurements performed with a high deposition rate will be influenced by the Fe atom dynamics. This phenomenon has been studied R. Belanger.

Susceptibilities in the perpendicular direction, the in-plane[001] direction and the in-plane $[\bar{1}10]$ direction have been measured at different temperatures from 255K to 385K and are displayed in Figure 4.5. Note that each curve represents a susceptibility measurement obtained as a film is grown. When different susceptibility components are plotted on the same graph, these are measurements were made as different films are grown in succession on one day. Measurements on different graph may be made months apart.

It is clear that the detailed shape of the curves is not reproducible. However, despite of the sensitivity to details of the film growth, there are important points of consistency. They are

- χ_{\perp} exhibits two peaks of variable relative size. In some cases, one the peaks is so small that it is difficult to observe. In other cases the peaks overlap to create a "shoulder".
- The peaks in χ_{\perp} at large coverage exhibit and\ exponential decay on the high coverage side, that varies as $\exp(At^{-\frac{3}{2}})$.
- A sharp peak in χ_{001} precedes the region of exponential decay.
- No signal is detected in $\chi_{[\bar{1}10]}$.

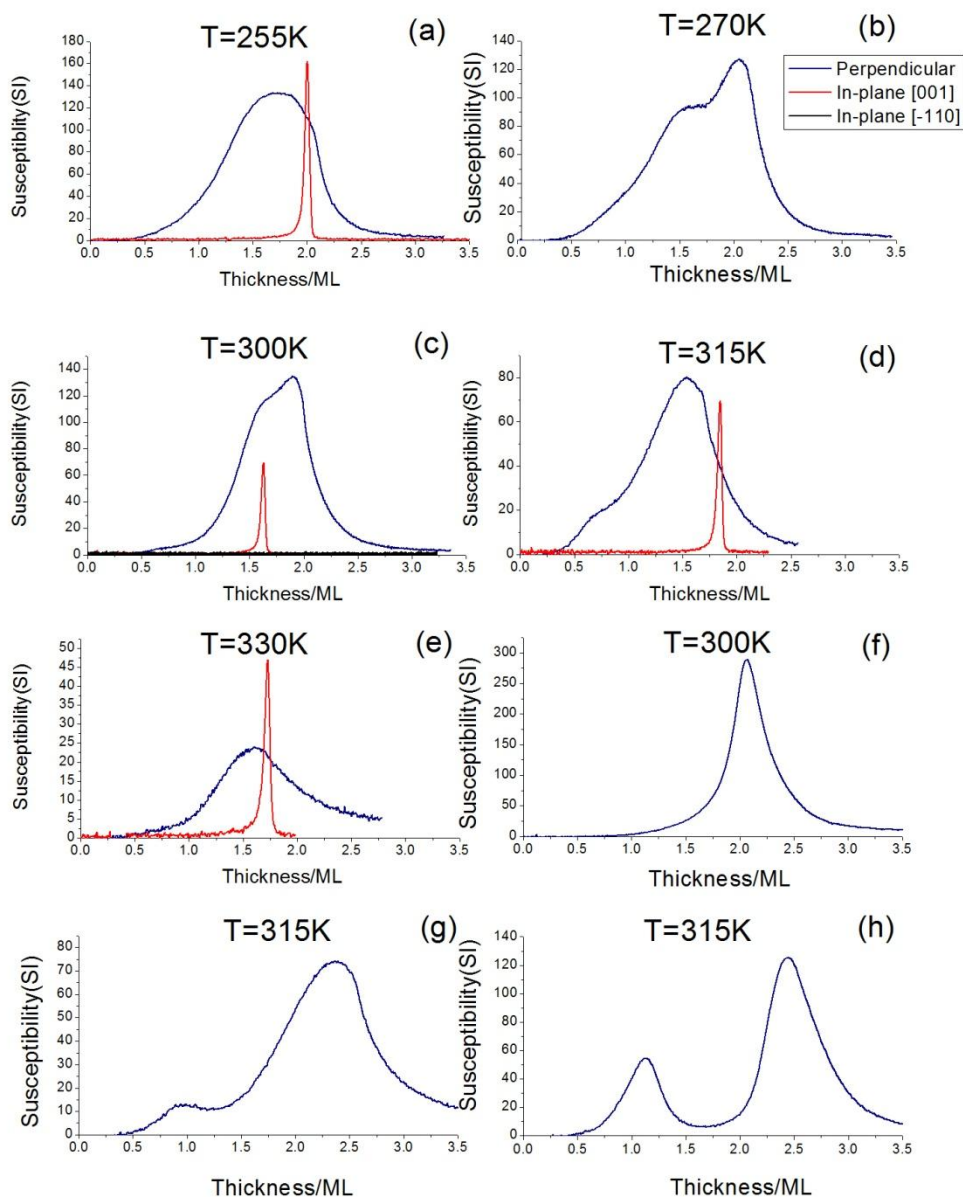


Figure 4.5 The susceptibility spectrum measured at different temperature. The χ_{\perp} presents two peaks with different relative sized. χ_{\perp} in (a)-(e) presents a shoulder shape. Other shapes of χ_{\perp} are presented in (f)-(h). Specifically, two χ_{\perp} peaks are well separated in (h). An exponential decay occurs in all χ_{\perp} at high coverage. χ_{001} peaks precede to the exponential decay are observed.

The following sections present a consistent interpretation of the data by

- a SRT from the perpendicular state, through a canted state that is aligned along [001].
- a susceptibility peak associated with the formation of a complete Fe layer

4.3 The continuous process of thickness driven SRT

Quantitative comparison to the model of a stripe domain state at canted phase show that the peak in χ_{\perp} and $\chi_{[001]}$ present a SRT

4.3.1 Exponential decay: the stripe domain state

Even though the two peaks in χ_{\perp} often overlap, it rarely affects the high thickness side of the 2nd peak. Figure 4.6 shows these data can be well fitted by the stripe domain model

$$\chi_{\perp} \sim C \exp \left[\sqrt{\frac{A_0 K_s b^2}{\Omega^2} \frac{1}{t^3}} \right] \text{ as derived in section 2.6.4.}$$

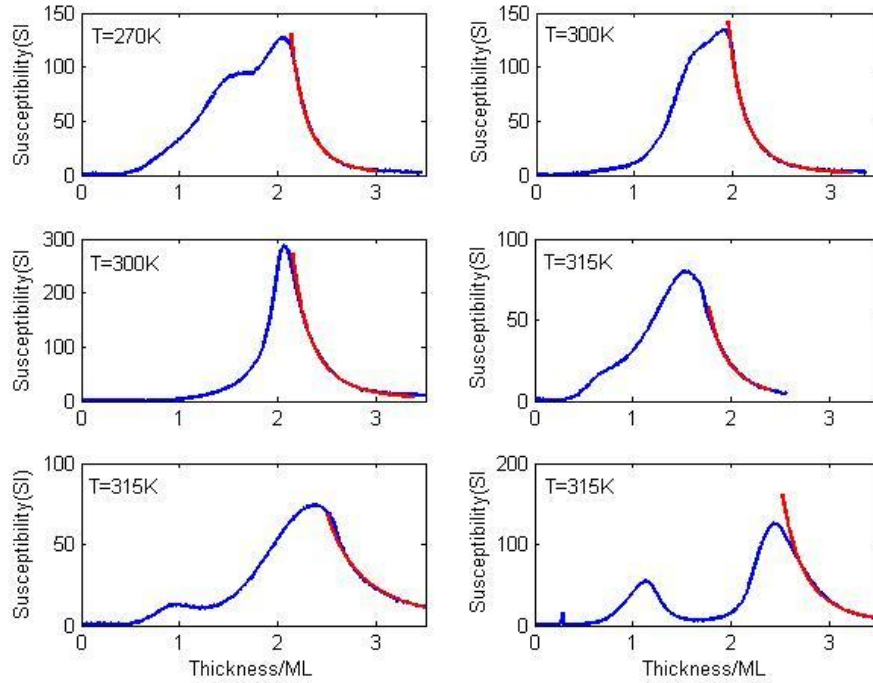


Figure 4.6 The fitting of the exponential decay. The blue lines are the experiment data and the red dash line is the fitting line. The exponential decay is well fitted by the stripe domain model that

$$\chi_{\perp} \sim C \exp \left[\sqrt{\frac{A_0 K_s b^2}{\Omega^2}} \frac{1}{t^3} \right]$$

This result is in agreement with many previous studies of the stripe domain state in the temperature driven SRT[7, 14].

4.3.2 The pinning effect

According to the stripe domain model, χ_{\perp} should diverge at low thickness if the domains move freely. However, the experimental data shows χ_{\perp} turns over and a peak is formed. This is the result of the pinning effect, which has been studied by M. Dunlavy and S. Arnold in the temperature driven SRT[15].

As we discussed, the susceptibility of a magnetic film in the stripe domain state comes from the domain wall motion. This motion can be strongly influenced by defects on the substrate. As Figure 4.7 shows, when the wall is pushed by an external magnetic field, it can be pinned by the defect. A relaxation time τ will be taken for the domain wall to escape from the pinning site. This relaxation time is correlated to the activation energy E_a and $\tau = \tau_0 \exp\left(\frac{E_a}{k_B T}\right)$.

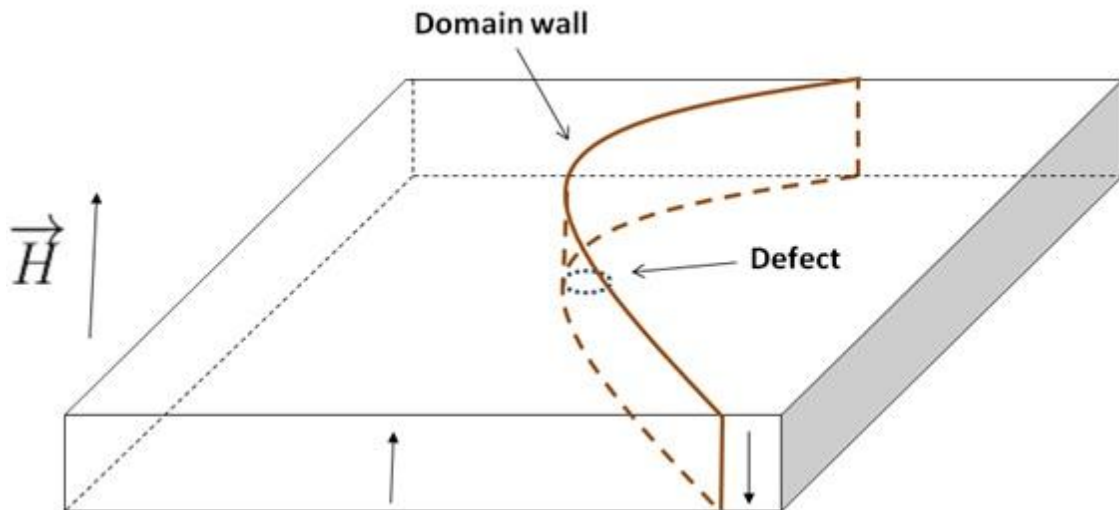


Figure 4.7 The domain wall is pinned by the defect. Domain wall can be pinned by defects. An activation energy is needed to escape

As the susceptibility is measured by applying an ac magnetic field, if the relaxation time is longer than the applied field period, the susceptibility will be suppressed.

One important defect in the Fe/2ML Ni(111)/W(110) system is the terrace structure on the surface of the W substrate, as Figure 3.2 shows. We have discussed that the domain walls have higher energy when the film is thicker. If the substrate is uniformly covered by the Ni

buffer and the Fe film, the Fe/2ML Ni film will be thicker at lower terrace areas. Thus an energy difference is created between domain walls on different levels of terraces. This energy difference is the activation energy for this model.

This energy difference is small in thicker films as the fractional change in the thickness is less significant and the activation energy is smaller. Then the domain walls can be moved freely and result in an exponential decay in susceptibility as the thickness increases. In thinner films, domain walls are pinned and the susceptibility is reduced.

Taking the pinning effect into consideration, the relation between the film thickness and the magnetic susceptibility becomes

$$\chi_{\perp} = \frac{1}{1 + \omega^2 \tau_0^2 \exp(Dt^{-\frac{3}{2}})} \cdot C \exp \left[\sqrt{\frac{A_0 K_s b^2}{\Omega^2} \frac{1}{t^3}} \right] \quad (4.10)$$

where the activation energy E_a is proportional to $t^{-\frac{3}{2}}$.

This model can be tested in χ_{\perp} data where the two peaks are well separated, such as in Figure 4.5 (e). As Figure 4.8 shows, The entire 2nd peak can be well fitted by the pinning effect model for a stripe domain state.

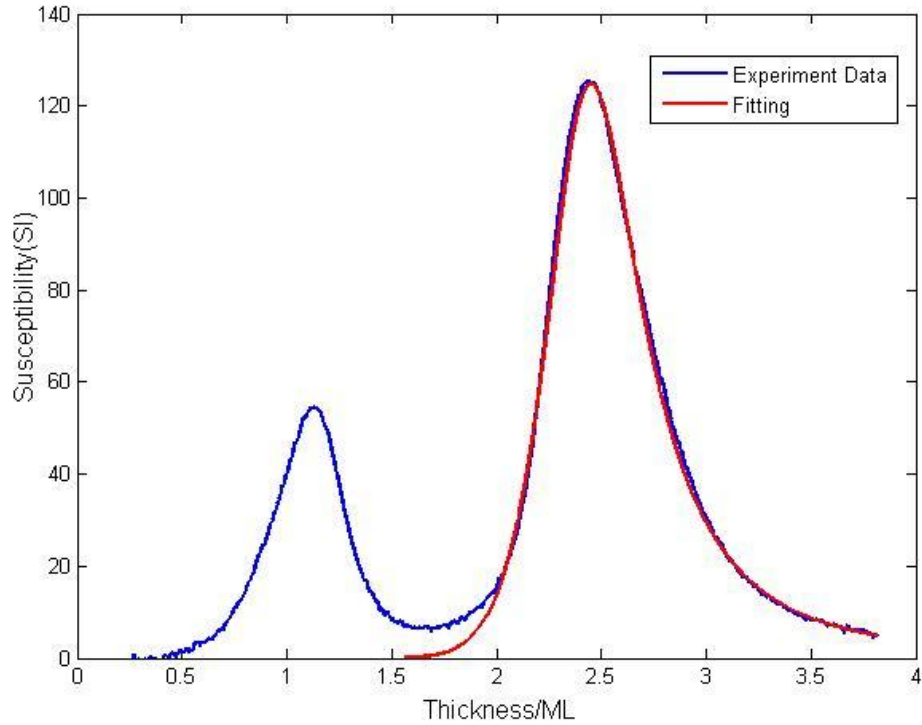


Figure 4.8 A typical susceptibility data presenting the pinning effect. The second peak is well fitted by the stripe domain model with pinning effect. Stripe pattern should occur before the peak.

Not every measurement of χ_{\perp} in Figure 4.5 can be fitted by this model, as the shape of the second peak varies. A possible explanation of this shape difference is the influence of defects other than the terrace structure on the W substrate, such as 3D islands and vacancies in the Ni buffer and Fe film. These defects will be especially important at thicknesses near and below 1ML. An extreme case of a defect in the film is an incomplete initial layer at $t \leq 1ML$. A completely different magnetic model is needed to describe the formation and coalescence of islands in this region. This is presented in section 4.4.1 where the first peak in χ_{\perp} is analyzed.

4.3.3 χ_{001} peak: the starting point of the canted state and the continuous SRT

As we discussed in section 2.7.3, the phase transition between the perpendicular state and the canted state will result in a strong in-plane susceptibility signal. The χ_{001} peak in the measurements show in Figure 4.5 is attributed to this phase transition. An order-disorder phase transition can result in a similar peak. However, the strong perpendicular signal after the peak occurs indicates the system maintained its magnetic ordering in the perpendicular direction, which excludes the possibility of the order-disorder transition. Thus a continuous perpendicular-canted phase transition is the only reasonable explanation for this susceptibility peak.

The continuous SRT is a combination of the canted state and stripe domain state. Figure 4.9 plots χ_{\perp} and $\chi_{[001]}$ obtained at 300K where the canted region and the stripe domain regions overlap.

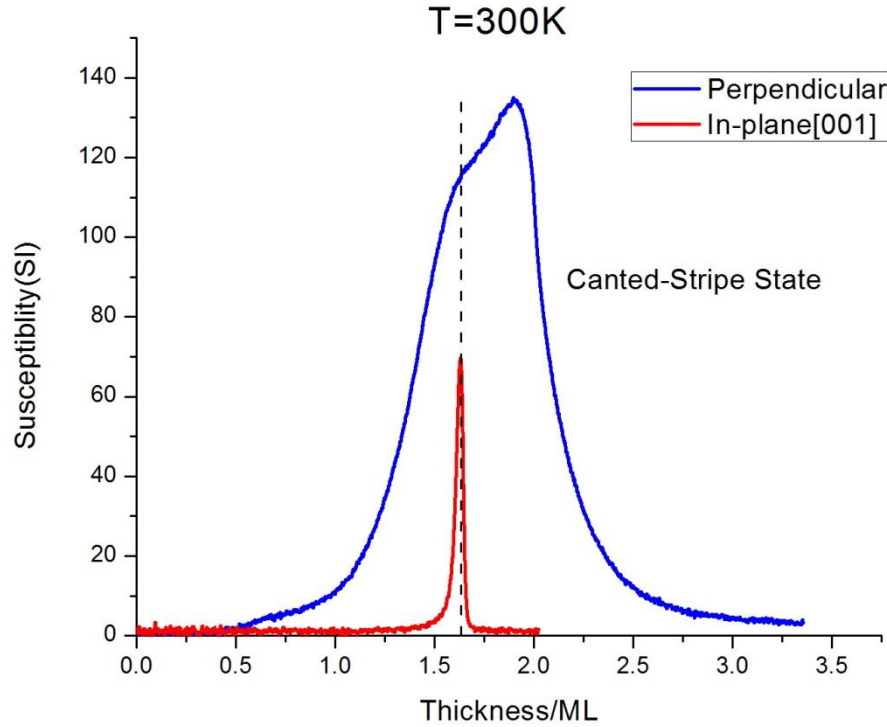


Figure 4.9 The perpendicular [111] susceptibility and the in-plane [001] susceptibility obtained at 300K. The sharp in-plane peak precedes the exponential decay. It indicates a canted stripe pattern above the in-plane transition peak.

Thus, during the continuous SRT process, the system should have a canted state with a stripe domain pattern. On one hand, the perpendicular components of the magnetization in the neighbouring domains are opposite. On the other hand, the in-plane component of each domain are all aligned in the stripe direction. A sketch of the canted-stripe model is displayed in Figure 4.10.

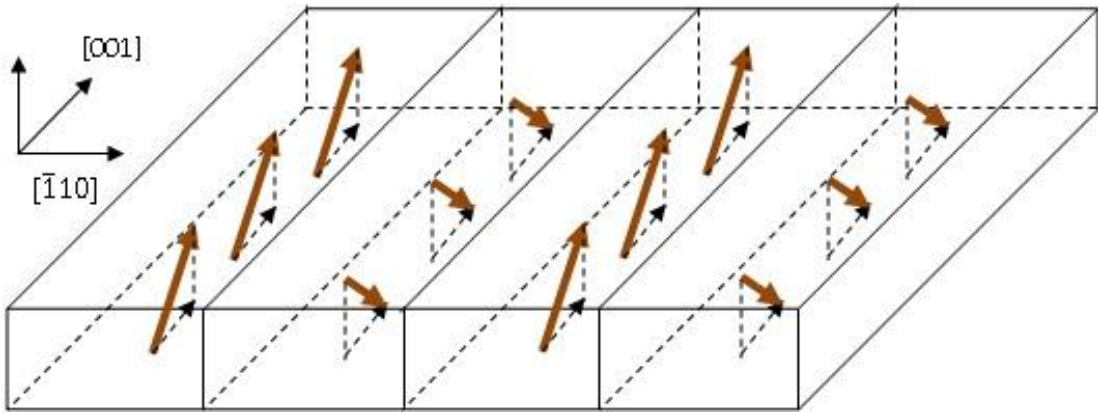


Figure 4.10 A sketch of the canted-stripe state. Magnetizations with same magnitude in different domains canted along the stripe direction. The perpendicular components in the neighboring domains are antiparallel. In-plane components in all domains have the same orientation along the stripe direction.

4.3.4 The in-plane [001] anisotropy

The fact that a peak occurs in $\chi_{[001]}$ instead of $\chi_{[\bar{1}10]}$ indicates that the in-plane components of the canted stripe phase are aligned by an in-plane [001] crystalline anisotropy. This is in agreement with studies of the temperature-driven SRT by Arnold. We have confirmed the result in 2 ways.

First, the Curies transition is observed in the [001] direction for a 4.5ML film with $T_C \approx 445K$, as Figure 4.11 shows. Thus, the magnetization has a [001] orientation in the in-plane ferromagnetic state.

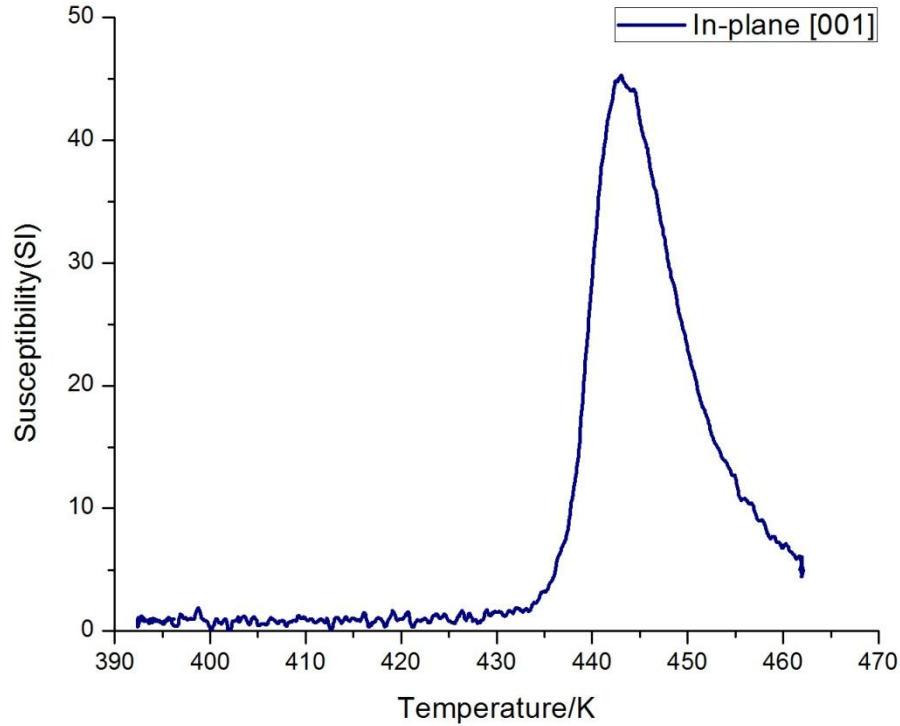


Figure 4.11 The Curie transition peak of a 4.5ML Fe film in the in-plane [001] direction.

Secondly, we performed another experiment which demonstrated the in-plane anisotropy. A 950Oe in-plane dc pulse field is applied on a 4.2ML Fe film at room temperature in both [001] and $[\bar{1}10]$ directions.. The magnetization will be reversed only when the remnant magnetization is opposite to the applied pulse field. As a result, the Kerr effect polarization angle will change and the SMOKE signal will have a step shape. Figure 4.12 presents the SMOKE signal when the dc field pulse was applied. Arrows indicates the pulse position and direction. The clear step shape is only obtained in the [001] direction, which indicates the [001] anisotropy.

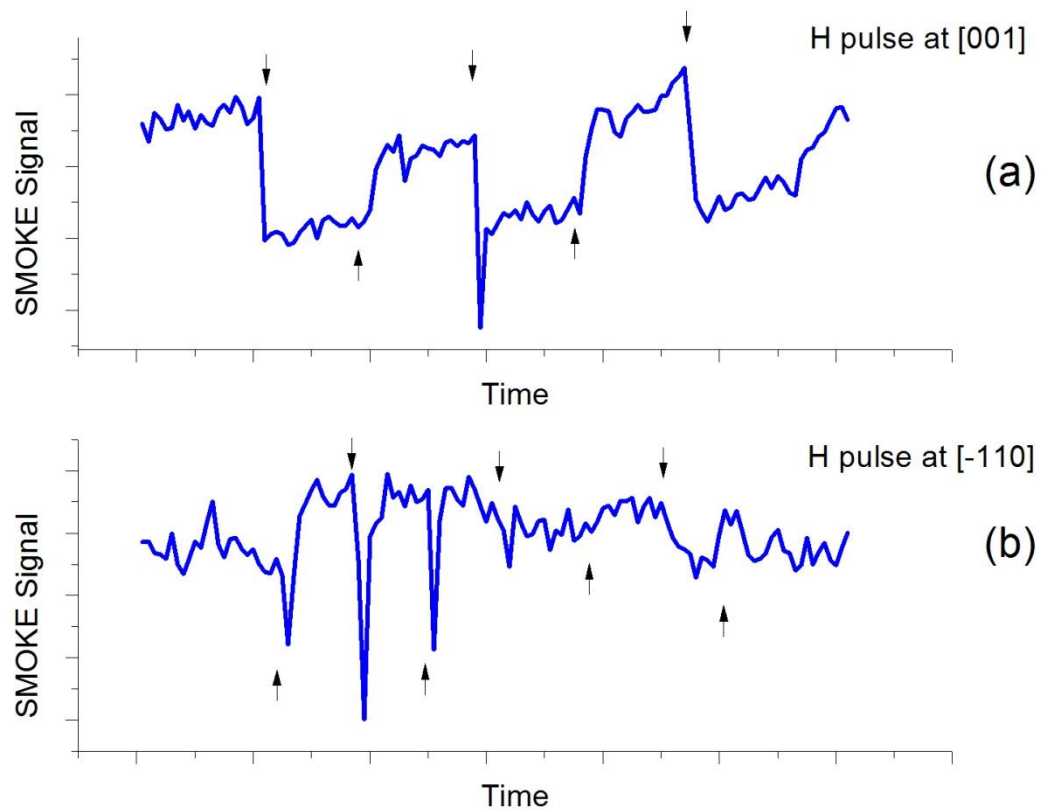


Figure 4.12 Figure 4.13 The SMOKE signals with DC field pulse: (a) the applied pulse field is in the $[001]$ direction. Pulses are mark by the arrows. The magnetization is flipped after each pulse and the clear steps in the SMOKE signal is observed in this direction; (b) the applied pulse field has $[\bar{1}10]$ direction. No clear step is observed.

The in-plane anisotropy aligns the stripes along the $[001]$ direction, as the canting direction of spins has to agree with the in-plane magnetization orientation. Then at the perpendicular-canted transition point, spins can be only wiggled along $[001]$. This agrees with the fact that the perpendicular-canted phase transition peak is observed in Figure 4.5 (c) and no peak is observed in $\chi_{[\bar{1}10]}$.

4.3.5 A sketch of continuous SRT

Based on the above discussions, Figure 4.14 sketches the process of the thickness driven SRT via the canted-stripe state. The magnetization with $\sin(\frac{\pi}{2} - \theta) = 1$, $\sin(\frac{\pi}{2} - \theta) = 0$, $\sin(\frac{\pi}{2} - \theta) = -1$ are presented by red, green and blue, respectively. Domain walls are present by the interchanging colors between each neighbouring stripes. The domain wall width is assumed to keep constant for convenient. Note in an actual SRT process, the domain wall width will increase.

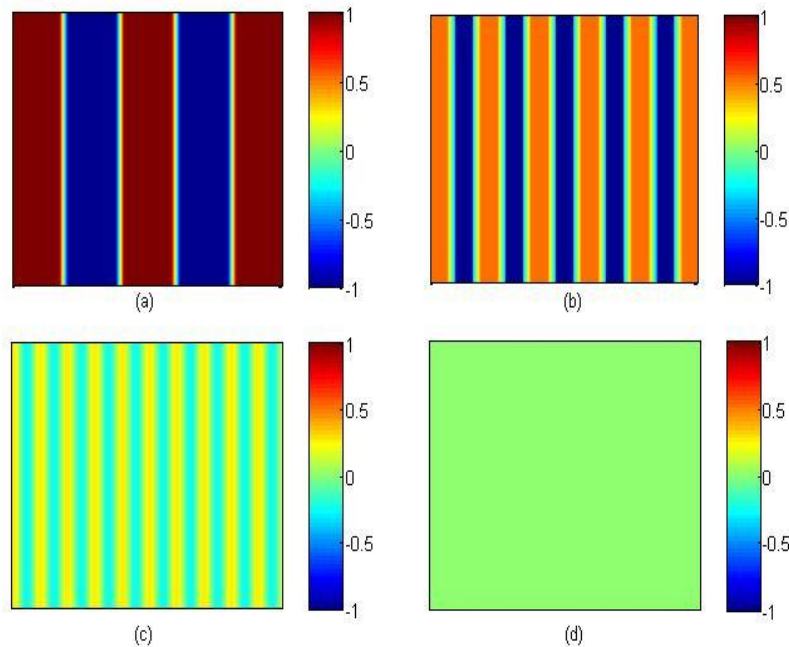


Figure 4.14 The change of stripe pattern in a unit area in x-y plane during the SRT process. The color scale presents the value of $\sin(\frac{\pi}{2} - \theta) = 1$. As the film thickness increase from (a) to (d), magnetizations fall into in-plane. Domain density increases while domains and domain walls emerge together.

As the thickness increases from Figure 4.14(a)-(d), the magnetization in each stripe gradually falls to the film surface. At the same time the domain density increases exponentially. Figure 4.14 (a) shows a clear boundary between the domains and the domain walls. As the direction difference between the neighbouring domains gets smaller, this boundary become ambiguous and the domain wall emerges with domains in the end of the SRT and the magnetization totally falls into the in-plane direction, like Figure 4.14(c)-(d) shows.

4.3.6 Approximate phase diagram of continuous SRT

The in-plane [001] susceptibility obtained at different temperatures is displayed in Figure 4.15

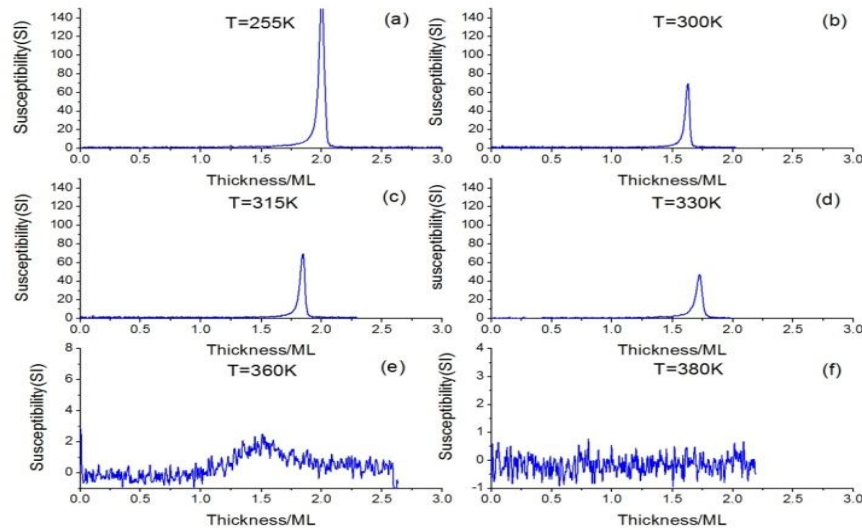


Figure 4.15 The in-plane [001] peaks obtained at different temperatures. The transition thickness changes with temperature. The peak magnitude decreases as temperature increases and disappeared at $T=380\text{K}$. It indicates a "disordering" process in perpendicular direction

An approximate phase diagram of the continuous SRT is plotted in Figure 4.16 based on the perpendicular-canted transition peak. The red line is the boundary between the perpendicular state and the canted state. The in-plane ferromagnetic state should be placed at the high thickness region on the right of the canted state. The boundary of the disorder state is plotted by a horizontal dash line, as it is an approximation based on the disappearance of the $\chi_{[001]}$ at 380K.

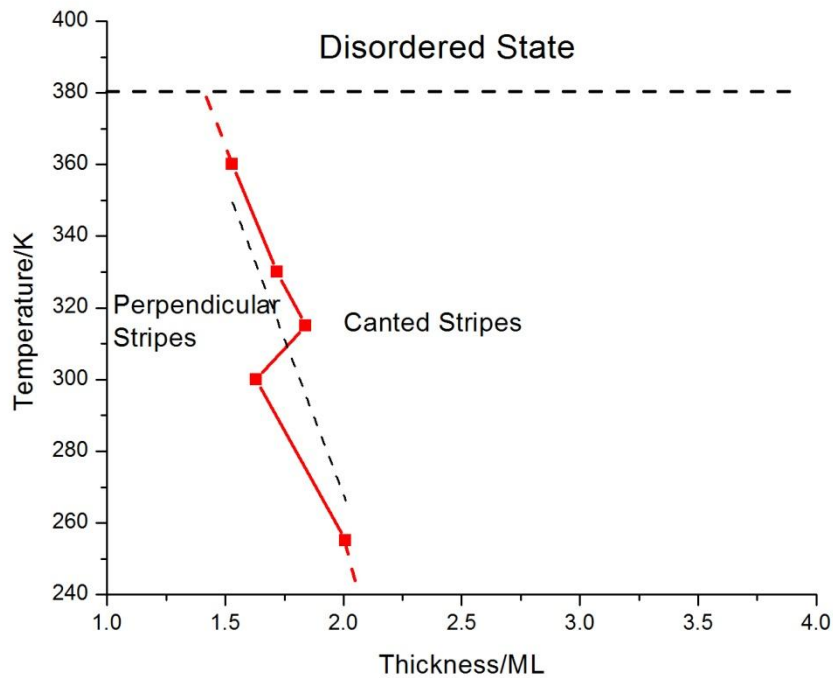


Figure 4.16 The approximate phase diagram. The transition line of perpendicular-canted state is approximately linear and fitted by $t_c = t_0 - \alpha T$. The system has a disorder state at high temperature. The transition line between the order-disorder state is unclear. An approximate dash line is used based on the fact that the perpendicular-canted state transition peak disappeared at $T=380\text{K}$.

We recall the perpendicular-canted transition occurs when

$$\widetilde{K}_1(T, t) = \frac{K_1(T)}{t} - \frac{1}{2}\mu_0 M_s^2 = 0 \quad (4.11)$$

Thus $K_1(T)$ can be written as

$$\begin{aligned} K_1(T) &= \frac{1}{2}\mu_0 M_s^2 t_c \\ &= \frac{1}{2}\mu_0 M_s^2 t_0 - \frac{1}{2}\mu_0 M_s^2 \alpha T \end{aligned} \quad (4.12)$$

Where the transition thickness t_c is fitted to a line as $t_c = t_0 - \alpha T$, in the data in Figure 4.16, with $t_0 = 8 \times 10^{-10} m \pm 1 \times 10^{-10} m$ and $\alpha = 1.1 \times 10^{-12} mK^{-1} \pm 0.4 \times 10^{-12} mK^{-1}$. The approximate relation of $K_1(T)$ can be written in the SI unit as

$$K_1(T) = [1.5 \pm 0.2 \times 10^{-3} - 2.1 \pm 0.8 \times 10^{-6} K^{-1} \cdot T] Jm^{-2} \quad (4.13)$$

Where the saturation magnetization for Fe is $M_s = 1752 emu/cm^3$ [9], and the thickness for one monolayer is $t = 2.8 \times 10^{-10} m/ML$.

For room temperature $T=300K$, the value of the anisotropy constant is $K_1 = 0.8 \pm 0.4 erg/cm^2$, which is approximately in agreement with the experimental value $K_1 = 0.69 erg/cm^2$ for a fcc (001) 5.7ML Fe/ 7ML Ag film [2]. This estimation only considered the saturation magnetization of Fe. In more accurate calculation, the magnetization of Ni should be considered too, which will make the value of K_1 smaller, as the Ni buffer has a smaller saturation magnetization.

In Figure 4.17 we plot the peak magnitudes versus temperature along the transition line. Notice that the thickness at each point is different. From 255K to 360K, the relation between the peak magnitude and the temperature is close to linear at the transition peak

disappeared at 380K.

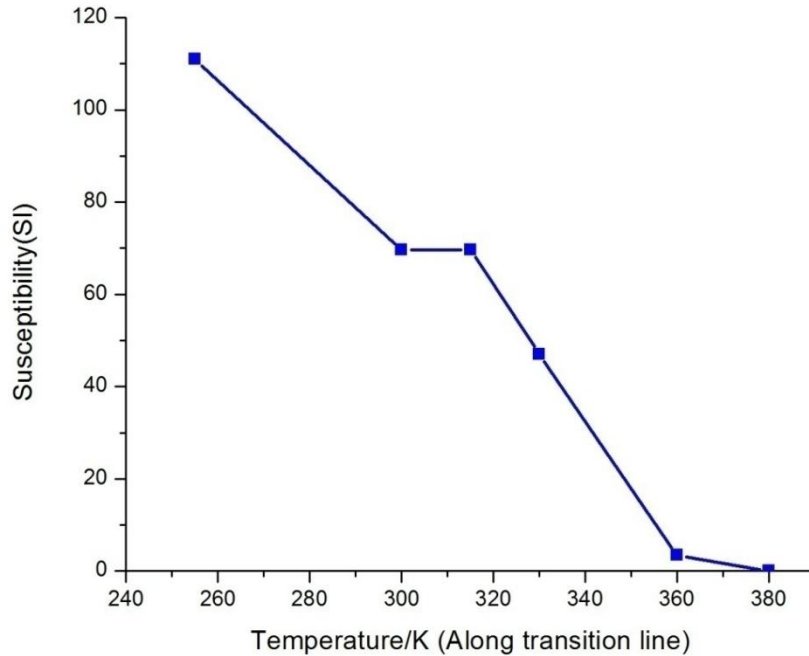


Figure 4.17 The magnitude of the in-plane [001] peak versus the temperature.

The disappearance of the transition peak indicates a disappearance of the stripe domain state. However, the linear decay of the peak magnitude with temperature indicates it is not a Curie transition, where thermal fluctuation overcome the exchange coupling, J . If it was a Curie transition, then $\chi_{[001]}$, which is proportional to the canting of the magnetization in a stripe by a applied field, would disappear like $M \sim (1 - \frac{T}{T_c})^\beta$. $\beta = \frac{1}{8}$ in 2D Ising model.

The transition is more likely described by thermal domain melting[34]. In the transition, the domain pattern fluctuates strongly because of thermal energy and changes into a maze

like pattern[35]. As the domain width decreases exponentially, there is no clear ordering in the system and the domain magnetization is close to zero.

4.4 Magnetism during the film formation

The first peak in χ_{\perp} which occurs at around 1ML shows the magnetic properties during the formation of the first layer Fe film. The variation of the relative size of the two peaks in χ_{\perp} could be the result of defects in the Ni buffer and Fe film. A quantitative model is used to explain the mechanism behind the first peak.

4.4.1 Influence of the defects in the Ni buffer

To study how defects influence χ_{\perp} , Ni buffers with 3D islands are made by changing the growth recipe. Instead of annealing at 1ML, a 1.5ML Ni film is annealed by the ordinary procedure. As discussed, Ni atoms on the second layer will form 3D islands during the annealing procedure. After that, another layer of Ni is deposited via the usual process.

Figure 4.18 presents the susceptibility spectra with these low quality Ni buffers. Figure 4.18(a) is for a high quality Ni buffer. It comes from Figure 4.5 (c) and is used as a control. Figure 4.18 (b)-(d) are taken at 315K from low quality films with 3D islands. These susceptibility spectra show completely different behaviours from part (a). Only one peak with a small size in χ_{\perp} remains. The $\chi_{[001]}$ transition peak is observed in Figure 4.18 (d) and the magnitude is significantly suppressed.

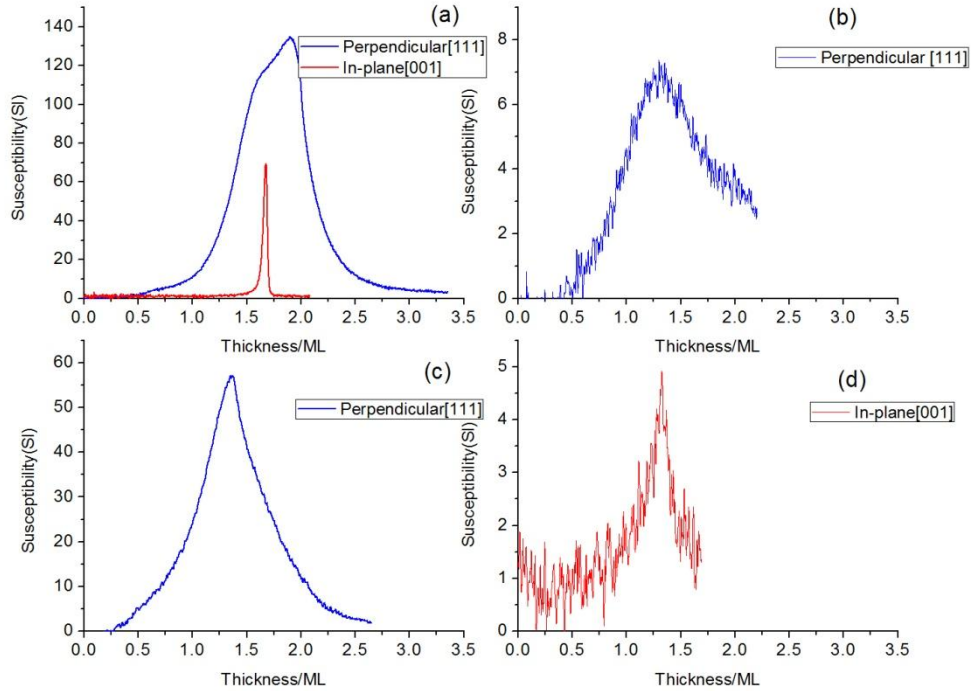


Figure 4.18 The influence of 3D islands on susceptibility. (a) from a high quality film used as the control. (b)-(d) are obtained at $T=315\text{K}$

The remaining χ_{\perp} peak is the first peak, or "shoulder" seen in the control data. Both the shoulders and the well-separate first χ_{\perp} peak in Figure 4.5 occurs between $1.0\text{ML} \sim 1.5\text{ML}$, which is in agreement with the location of the remaining χ_{\perp} peaks in Figure 4.18 (b) and (c). The second peak vanishes in the low quality films because the pinning effects are greatly enhanced by defects in low quality films and domain walls cannot move. We speculate that the pinning is so strong that it will not permit the perpendicular domains to arrange in a stripe pattern. Thus the peak in $\chi_{[001]}$ at the transition is broad and weak.

Since the domain walls cannot move, the remaining first peak in χ_{\perp} is likely due to isolated Fe islands. It should be due to the superparamagnetization response of the islands as they form and coalesce into a film at thickness $t \lesssim 1ML$.

In more ordinary samples, a relatively small number of defects may not have as large an influence as is seen in these extreme conditions, but will still influence the shape of χ_{\perp} by changing the relative strength of the two peaks.

4.4.2 The magnetic island model for the first layer Fe film formation

The first peak in χ_{\perp} is related to the magnetic properties during the first layer Fe film formation. To explain the mechanism behind this peak, a model is built based on the formation of superparamagnetic islands.

The idea for this model comes from J. Amar's study of first layer film formation[36]. According to his work, 1ML islands with different sizes are formed when $t \leq 1ML$. The number of islands, N_{sn} with the number of atoms, s , changes with the coverage. We also find these islands should have a perpendicular magnetization based on H. J. Elmers' simulation[37].

Thus, the magnetic islands model is built as follows. One atomic layer islands with perpendicular magnetization are formed during the film formation. The susceptibility signal in this model comes from reversing the magnetization in the single-domain islands, as Figure 4.19 shows. A perpendicular external field can reverse the magnetization and induce a superparamagnetic response.

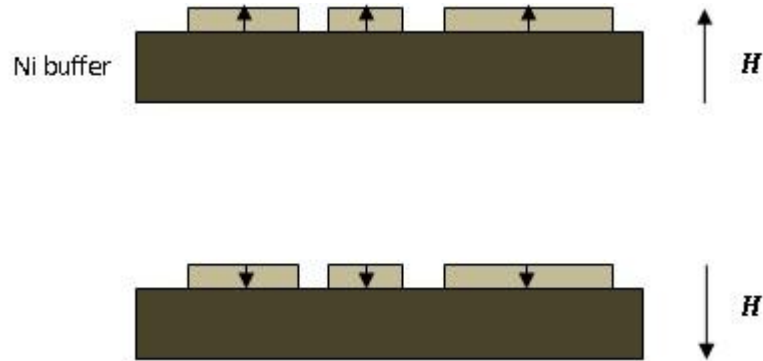


Figure 4.19 The model with perpendicular magnetized islands is used to explain the first peak. Monolayer islands with perpendicular magnetization is formed. The susceptibility comes from reversing the magnetization. The activation energy comes from the anisotropy.

The susceptibility of the islands with size s under a small external field is

$$\chi_0^s = \frac{s^2 m^2 N_s(\theta)}{k_B T} \quad (4.14)$$

where $N_s(\theta)$ is the density of islands with size s , which depends on the coverage θ .

An activation energy E_a from the perpendicular anisotropy is required to flip the magnetization.

$$E_a = K \cdot s \quad (4.15)$$

where the K is defined as the anisotropy energy per atom. Similar to the pinning effect model, a relaxation time τ is related to the activation energy, which will suppress the susceptibility in the ac measurement

$$\tau_s = \tau_0 \exp\left(\frac{K \cdot s}{k_B T}\right) \quad (4.16)$$

and the real component of the ac susceptibility for islands with size s is

$$Re\chi^s = \frac{\chi_0^s}{1+\omega^2\tau_s^2} \quad (4.17)$$

The total ac susceptibility is the summation of $Re\chi^s$ among $s_c < s < s_L$. The limits of s comes from two effects. s_L is the limitation for large islands. The activation energy is proportional to the island size. Islands larger than s_L begin to coalesce and form a very large net work. As they coalesce, immediately removed from the island distribution in Amar's model. Thus only islands with sized s smaller than s_L make contribution to total susceptibility. The lower bond s_c comes from the fact that islands have to be larger than a critical size to have a perpendicular magnetization which is demonstrated by H. J. Elmers' simulation[37]. This is because the Ni buffer has an in-plane magnetization.

Then, the real component of the total ac susceptibility can be written as

$$Re\chi = \frac{m^2}{k_B T} \sum_{s_c < s < s_L} \frac{s^2 N_s(\theta)}{1+\omega^2\tau_s^2} \quad (4.18)$$

According to J. Amar and *et al*[36], the distribution of $N_s(\theta)$ is

$$N_s(\theta) = \frac{\theta}{S^2} f(u) \quad (4.19)$$

Where $u = \frac{s}{S}$. Capital S is the average island size $S = \frac{\sum_s s N_s(\theta)}{\sum_s N_s(\theta)}$. f is the distribution function which is normalized to one

$$f(u) = C u e^{-au^{1/a}} \quad (4.20)$$

C and a are constants. According to Amar *et. al*[36], for $\theta \gtrsim 0.1ML$ atoms accumulate on existing islands, rather than forming new islands.

Combining these, the coverage dependent susceptibility can be written as[38]

$$Re\chi = A\theta^2 \int_{a/\theta}^{b/\theta} u^2 f(u) \frac{1}{1 + \omega^2 \tau_0^2 \exp(B \cdot \theta u)} du \quad (4.21)$$

where A , B , a and b are constants.

A susceptibility peak is predicted by this model, as Figure 4.20 shows. Unfortunately, the shape of this model does not agree quantitatively with the original data.

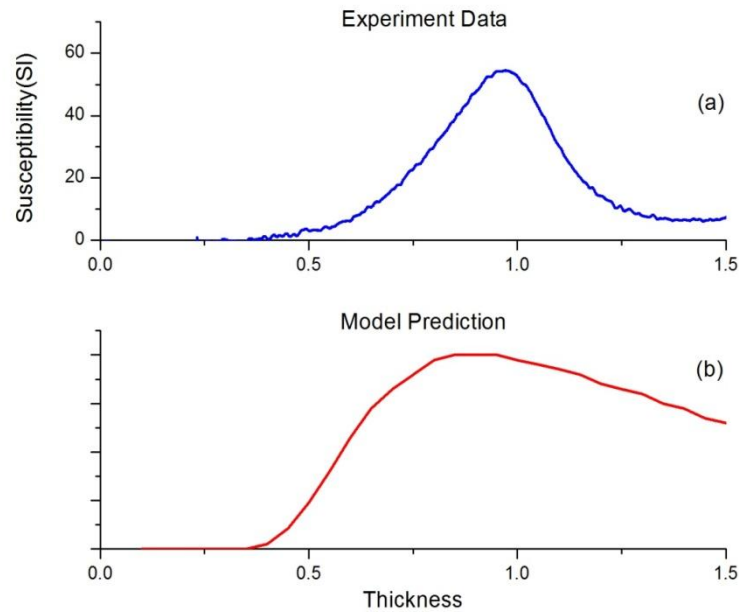


Figure 4.20 The (a) experiment data of the first peak comparing with (b) the model predicted first peak. The model result in a much wider peak comparing to the experiment data.

The model can be improved from two aspects. First, as seen in Figure 4.21, where the first peak is well defined, the experimental data increases as $\theta^4 \sim \theta^5$. Second, to cut off the peak more sharply, the activation energy should vary as a higher power ($\sim \theta^2$) of θ . It is not clear what microscopic model has this characteristics.

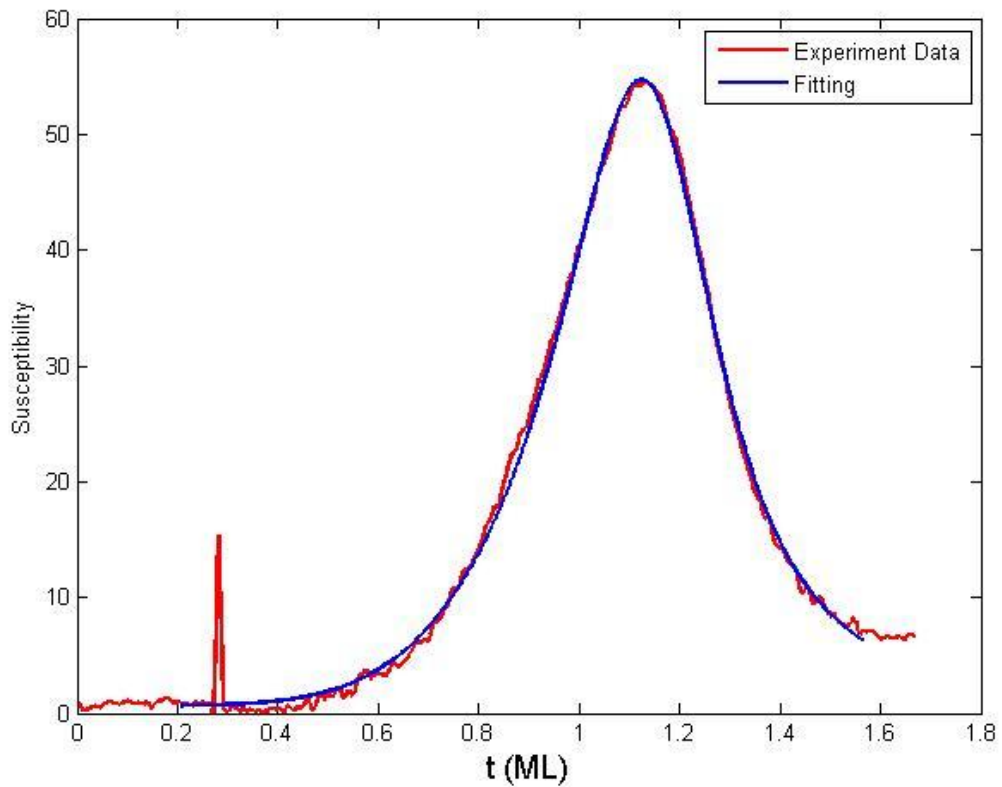


Figure 4.21 The fit of the first peak. To fit the data, χ_0 should follow $\theta^4 \sim \theta^5$ and the activation energy should follow θ^2 . The microscopic mechanism of these factors is unclear.

Chapter 5. Conclusions

The temperature driven SRT of Fe/2ML Ni/W(110) has been studied by previous members of our group. The stripe domain state and the pinning effect during the SRT process was well discussed. In this thesis, the thickness driven SRT is studied by SMOKE susceptibility measurement. This new point of view provides more information about the details of SRT process.

The χ_{\perp} spectrum has two peaks with variable relative position and size. Similar to the temperature driven SRT, an exponential decay observed in all measurements is identified as the stripe domain state. In some cases, where the two peaks are clearly separated, the second peak also agrees with the pinning effect model. A possible explanation for the variety of χ_{\perp} spectrum shapes is the influence of defects in the Fe films and Ni buffers, like 3D islands and vacancies. However, further experimental evidence is needed to demonstrate this assumption.

The thickness driven SRT is a continuous process. This is demonstrated by the sharp peak observed in $\chi_{[001]}$ spectra. According to theoretical studies of the SRT in anisotropy space, this peak is the result of the phase transition between the perpendicular state and canted state. Thus, the perpendicular magnetization falls to the in-plane direction gradually via the canted state. Comparing $\chi_{[001]}$ with χ_{\perp} , the canted state overlaps with the stripe domain state. This indicates that the stripe pattern remains in the canted state and a canted-stripe state occurs during the SRT process.

$\chi_{[001]}$ is measured at different temperature from 255K to 380K and an approximate

temperature versus thickness phase diagram of the perpendicular-canted phase transition is plotted. The transition line has a large slope. This might explain why the signal from this transition is not significant in measurements of the temperature driven SRT. The temperature dependence of the anisotropy factor $K_1(T)$ is found by fitting the transition line linearly.

The magnitude of the $\chi_{[001]}$ peak decays linearly along the transition line as the temperature increases and disappears between 360K to 380K. Obviously, this is the result of the thermal fluctuation, but the linear relation excludes it from the standard order-disorder Curie transition. A possible explanation is a domain melting process where domain walls merge with domains.

A magnetic island model is built to explain the first χ_{\perp} peak when the two peaks are clearly separated. However, the shape of the χ_{\perp} peak predicted by the model is not in quantitative agreement with the experiment data. Thus, the detailed mechanism behind the first peak and the magnetization properties during the first layer Fe film formation remain unclear. More study of the first peak is required.

Bibliography

- [1] L. Neel, J. Phys. Radium **15**, 225 (1954).
- [2] B. Heinrich, and J. F. Cochran, Adv. Phys **42**, 523 (1993).
- [3] D. P. Pappas, K. Kamper, and H. Hopster, Phys. Rev. Lett. **64**, 3179 (1990).
- [4] C. Garreau *et al.*, Phys. Rev. B **53**, 1083 (1996).
- [5] A. B. Kashuba, and V. L. Pokrovsky, Phys. Rev. B **48**, 10335 (1993).
- [6] Y. Millev, and J. Kirschner, Phys.Rev.B **54**, 4137 (1996).
- [7] C. S. Arnold, H. L. Johnston, and D.Venus, Phys. Rev. B **56**, 8169 (1997).
- [8] S. Blundell, *Magnetism in Condensed Matter* (Oxford University Press, 2001).
- [9] N. W. Ashcroft, and N. D. Mermin, *Solid State Physics* Thomson Learning, 1976).
- [10] R. M. White, *Quantum Theory of Magnetism* (Springer, 2006).
- [11] J. Kessler, *Polarized Electrons* (Springer, Berlin Heidelberg, 1985).
- [12] S. Chikazumi, (Oxford University Press, 1997).
- [13] Y. Yafet, and E. M. Gyorgy, Phys.Rev.B **38**, 9145 (1988).
- [14] C. Won *et al.*, Phys.Rev.B **71** (2005).
- [15] D. Venus, C. S. Arnold, and M. Dunlavy, Phys. Rev. B **60**, 9607 (1999).

- [16] A. E. Austin, E. Adelson, and W. H. Cloud, *Journal of Applied Physics* **33**, 1356 (1964).
- [17] H. S. Jarrett *et al.*, *J. Appl. Phys.* **32**, S57 (1961).
- [18] M. K. Wilkinson, N. S. Gingrich, and a. C. G. Shill, *J.Phys.Chem.Solids* **2**, 289 (1957).
- [19] R. W. Houghton, and W. Weyhmann, *Phys. Rev. Lett.* **20**, 842 (1968).
- [20] G. R. Davidson *et al.*, *Phys.Rev.B* **12**, 1681 (1975).
- [21] H. Ohldag *et al.*, *Phys. Rev. Lett.* **86**, 2878 (2001).
- [22] Y. Millev, and M. Fähnle, *Phys.Rev.B* **52**, 4336 (1995).
- [23] J. R. MacDonald, *Proc. Phys. Soc London, Sect. A* **64**, 968 (1951).
- [24] N. M. Abu-Libdeh, *PhD Thesis* (McMaster University, 2010).
- [25] C. S. Arnold, *PhD Thesis* (McMaster University, 1997).
- [26] M. Wutting, and X. Liu, *Ultrathin Metal films: Magnetic and Structural Properties* (Springer-Verlag, Berlin, 2004).
- [27] C. S. Arnold, and D.Venus, *Review of Scientific Instruments* **66**, 3280 (1995).
- [28] K. Fritsch, *M.Sc Thesis* (McMaster University, 2008).
- [29] H. L. Johnston, C. S. Arnold, and D. Venus, *Phys. Rev. B* **55**, 13221 (1997).
- [30] M. T. Kief, and W. F. Egelhoff, *Phys. Rev. B* **47**, 10785 (1993).
- [31] H. Johnson, *PhD Thesis* (McMaster University, 1997).
- [32] M. J. Dunlavy, and D. Venus, *Phys. Rev. B* **62**, 5786 (2000).
- [33] D. Sander *et al.*, *J. Appl. Phys.* **81**, 4702 (1997).

[34] N. Bergeard *et al.*, Phys. Rev. B **86**, 094431 (2012).

[35] R. Zdyb, and E. Bauer, Phys. Rev. B **67**, 134420 (2003).

[36] J. G. Amar, and F. Family, Phys. Rev. Lett. **74**, 2066 (1994).

[37] H. J. Elmers, Journal of Magnetism and Magnetic Materials **185**, 274 (1997).

[38] D. Venus.